Design of highly efficient semi-transparent perovskite/organic tandem solar cells

Daniele Rossi[1], Karen Forberich[2,3], Fabio Matteocci[1], Matthias Auf der Maur[1], Hans-Joachim Egelhaaf[2,3], Christoph Brabec[2,3] and Aldo Di Carlo[1,3,*]

[1]CHOSE (Centre for Hybrid and Organic Solar Energy), Department of Electronic Engineering, University of Rome "Tor Vergata", 00133, Rome, Italy

[2]Forschungszentrum Jülich GmbH, Helmholtz-Institut Erlangen-Nürnberg für Erneuerbare Energien (IEK-11) Abteilung Hochdurchsatzmethoden in der Photovoltaik (ZAE-Kooperation) Immerwahrstr. 2, 91058 Erlangen

[3]Institute of Materials for Electronics and Energy Technology (i-MEET), Friedrich-Alexander Universität Erlangen-Nürnberg (FAU) Martensstraße 7, Erlangen, D-91058, Germany.

[4]National Research Council (CNR), Institute of Structure of Matter (ISM), 00133, Rome, Italy

[*]Corresponding Author: aldo.dicarlo@uniroma2.it

Abstract

Solar cells transparent in the visible range are highly requested for integration in see-through photovoltaic (PV) applications such as building glass façades or green-house roofs. The development of advanced transparent PV can fully exploit the tandem technology where the top cell absorb the near-ultraviolet solar spectrum while the bottom the near-infrared part. In this work we consider a possible implementation of this tandem PV paradigm, namely the tandem structure composed by a high-band gap halide perovskite solar cell and a low-band gap organic solar cell. Electro-optical simulation results based on parameters calibrated on experimental data shows that efficiency of 15% can be achieved with Average Visual Transmittance above 50%. This can be obtained considering the halide perovskite with mixed Clorine and Bromine anions, a non-fullerene based bulk heterojunction, a well calibrated light management and a three terminal configuration of the tandem.

Introduction

Building-Integrated Photovoltaics (BIPV) represents one of the most effective and innovative solutions capable to meet the Nearly Zero Energy Building (NZEB) policy widely promoted in the last decades by the European Union [1]. In this context, transparent photovoltaic (TPV) technologies offer an additional opportunity to generate electricity through see-trough glass façades and windows. TPV could indeed guarantee good power conversion efficiency (PCE) and average visible transmittance (AVT) of over 50%, as often required in facades and window applications [1]. Over the years, several TPV approaches have been proposed. The use of thin films can be exploited to reduce the absorption in the visible range. As an alternative wavelength-selective approach, highly efficient ultra-violet (UV) and near-infrared (NIR) photoactive materials can be employed and, in particular, combined to reduce absorption in the visible range and consequently increase the AVT.

As fully organic semi-transparent solar cells have recently attracted great attention due to the high efficiency reported [2]–[4], semi-transparent tandem solar cells represent a promising candidate for new efficiency/AVT breakthroughs. In tandem structures, solar cells consisting of two or multiple photoactive layers with different bandgaps are used to selectively absorb different wavelength regions of the solar spectrum. Furthermore, it has been demonstrated that tandem architectures provide better light management than single cell devices, allowing to reduce the total loss induced by reflection and parasitic absorption [5]. To this end, the ease in bandgap tuning of a wide class of organic materials, such as the low bandgap NIR absorbing small molecules and polymers, and of high bandgap perovskites for UV absorption, such as methylammonium and formamidinium lead bromide/chloride ($MAPbBr_{3-x}Cl_x$ and $FAPbBr_{3-x}Cl_x$), makes these materials suitable for semi-transparent tandem photovoltaics applications [6]. This is demonstrated by the record efficiency of 9.8% [7] for a semi-transparent organic solar cell (ST-OSC) based on the PTB7-Th:FOIC:$PC_{71}BM$ bulk heterojunction, and the 7.5% [8] for a $FAPbBr_{2.81}Cl_{0.19}$ based semi-transparent perovskite solar cell (ST-PSC).

In the last decade, the PCE and AVT of semi-transparent tandem solar cells have been dramatically improved due to the choice of innovative organic and hybrid absorbers and their optimization in terms

of thickness and coating techniques. In fact, the efficiency of 3.07% and AVT = 40% obtained by employing low and high bandgap solid state dye sensitized solar cells (SS-DSSC) [9], have been rapidly surpassed by fully organic tandem devices (UV-OSC/NIR-OSC) with performance increased up to 8% and AVT = 45% [10], and more recently achieving the current record by using perovskite and organic solar cells (UV-PSC/NIR-OSC) showing PCE = 10.83% and AVT = 52.9% [8].

In this work, we present a theoretical study of the design criteria for the realization of highly efficient UV-NIR selective semi-transparent tandem solar cells for BIPV applications. The main objective is to demonstrate that UV-NIR selective tandem solar cells resulting from combining PSC and OSC allow to reach a ground-breaking PCE value of over 15% while keeping the AVT > 50%. The study is oriented to find the best trade-off between AVT and PCE compatible with the available device stacks and the related technology, and at the same time to preserve important features for real-life applications such as color neutral appearance and color temperature.

Electro-optical modeling

The performance of the single-junction and tandem solar cells is estimated by electro-optical simulations. A transfer matrix method (TMM) [11] based algorithm is used to model the electromagnetic field in the stacked devices as

$$\begin{bmatrix} E_T^+ \\ 0 \end{bmatrix} = \mathbf{I}_{0,1} \prod_{j=1}^{N} \mathbf{M}_j \cdot \mathbf{I}_{j,j+1} \begin{bmatrix} E_0^+ \\ E_R^- \end{bmatrix}, \quad (1)$$

where E_0^+ represents the incident electromagnetic field, while E_T^+ and E_R^- represent the transmitted and reflected field components, respectively. $\mathbf{M}_j$ and $\mathbf{I}_{j,j+1}$ are the transfer matrices describing propagation through the *i*-th layer and transmission from layer *j* to *j*+1, respectively, and are given by

$$\mathbf{M}_j = \begin{bmatrix} e^{-i\frac{2\pi}{\lambda}\tilde{n}_j t_j} & 0 \\ 0 & e^{i\frac{2\pi}{\lambda}\tilde{n}_j t_j} \end{bmatrix}$$

$$\mathbf{I}_{j,j+1} = \frac{1}{1 + r_{j,j+1}} \begin{bmatrix} 1 & r_{j,j+1} \\ r_{j,j+1} & 1 \end{bmatrix}$$

where $\tilde{n} = n_0 + ik$and t_j are the complex refractive index and thickness of layer *j*, respectively, and $r_{j,j+1}$ is the reflection coefficient at the interface.

Given the thickness and complex refractive index ($\tilde{n} = n_0 + ik$) of each of the layers, the product of j-th material layer's $\mathbf{M}_j$ and interface $\mathbf{I}_{j,j+1}$ transfer matrices allows estimating the coherent absorbance A(λ), transmittance T(λ) and reflectance R(λ). The calculation of the reflected, confined and transmitted optical field represents the key modeling step for the estimation of both the ideal photocurrent J_{sc}, with Internal Quantum Efficiency (IQE) equal to 100%, and AVT [1], given by the following formulas

$$J_{sc} = q \int_0^L G(x)dx = q \int_0^L \int_{\lambda_{min}}^{\lambda_{max}} \frac{1}{\hbar\omega} \cdot \frac{2\pi k}{\lambda} \cdot c_0 \varepsilon_0 n_0 |E(x)|^2 d\lambda dx \quad (2a)$$

$$AVT[\%] = \frac{\sum_{\lambda=380nm}^{780nm} S_\lambda T(\lambda) V(\lambda) \Delta\lambda}{\sum_{\lambda=380nm}^{780nm} S_\lambda V(\lambda) \Delta\lambda} \quad (2b)$$

E(x) in Eq. (2a) is the electromagnetic field within the active region of the solar cell, determining the generation rate profile *G(x)*. *L* is the total thickness of the active region. *k* and n_0 represent the position and wavelength dependent extinction coefficient and refractive index, respectively, while the integration limits λ_{min}, λ_{max} indicate the range of wavelengths accounted for. In Eq. (2b), the S_λ and $V(\lambda)$ are the AM1.5 solar spectrum and photopic eye sensitivity function, respectively. For the calculation of the AVT only the spectral range from 380-780 nm is considered. Although the TMM provides a detailed optical description of the device, it can only provide the upper limit of the solar cell performance, since it in fact neglects the electrical losses. For this reason charge transport calculations are performed by using the TiberCAD multiscale simulation software [12] based on the drift-diffusion (DD) model as given in Eq. (3a).

$$\nabla \cdot (\varepsilon \nabla \varphi) = -\rho \quad (3a)$$

$$\nabla \cdot (\mu_n n \nabla \Phi_n) = -R + G \quad (3b)$$

$$\nabla \cdot (\mu_p p \nabla \Phi_p) = R - G \quad (3c)$$

Poisson's equation (3a) determines the electrostatic potential (φ) from the total charge density (ρ), while the continuity equations in (3a)(b-c) describe the carrier transport in terms of carrier fluxes driven by the gradients of the quasi-Fermi potentials (Φ_n, Φ_p) and proportional to the carrier mobilities (μ_e, μ_p) and densities (n,p). G and R represent the total net generation and recombination rates. The first is directly extracted from TMM calculations, while the second includes the most relevant mechanisms such as the trap-mediated (Shockley-Read-Hall) and bimolecular (radiative and interfacial) recombination. The model allows to calculate the JV characteristic of the solar cell from which the main photovoltaic performance parameters such as short-circuit current density (J_{SC}), open-circuit voltage (V_{OC}), fill factor (FF) and power conversion efficiency (PCE) can be readily obtained.

Results and discussion

The purpose of this work is to define the design guidelines to maximize the power conversion efficiency of a tandem device with AVT $\geq$ 50, considering also aesthetical aspects such as the color perception by the human eye, quantified in terms of the Color Rendering Index (CRI).

We first wanted to get a better understanding of how efficiency and AVT depend on basic absorber properties such as bandgap and shape of the absorption spectrum. To achieve this goal, we performed TMM simulations in which the PSC and the OSC absorber are modeled by simplified rectangular absorption spectra with variable absorption onset. To better represent realistic OSC materials, their absorption spectra is divided into two separate bands with small variable absorption in the visible region and high absorption in the infrared region. For the perovskite and the second OSC band, the combination of extinction coefficient k and absorber thickness was chosen so that absorption is saturated. The other materials in the stack are based on a typical architecture, which is compatible

with up-scaling to larger areas, and described by optical constants from the literature or our own measurements (**Figure S1**). With respect to the stack, we chose the 4T architecture as the most general one. In order to estimate efficiency values from these optical simulations, we furthermore assumed IQE = 1, FF = 0.8 and a V_{OC} corresponding to 80% of the Shockley-Queisser limit for the PSC device as well as IQE = 0.9, FF = 0.7 and V_{OC} = 0.8V for an exemplary absorption cutoff of 1100 nm for the OSC device. PCE and AVT for low (~10%) absorption in the first OPV band are displayed in **Figure 1**. These results illustrate the inherent tradeoff between high PCE on the one hand, which can be obtained for PSC cutoffs corresponding to lower bandgaps and high OSC absorption in the visible region, and high AVT on the other hand which is only possible if absorption in the visible region, most notably between 500 nm and 600 nm, is as low as possible. **Figure 1d** shows in a binary plot how exemplary values of PCE = 15% and AVT = 50 % can be achieved for the chosen parameters. Results for higher absorption (~30% and ~50%) in the first OSC band shown in **Figure S1** show that these PCE and AVT can no longer be achieved simultaneously due to a strong decrease in AVT, underlining the requirement of low absorption in the first OSC band.

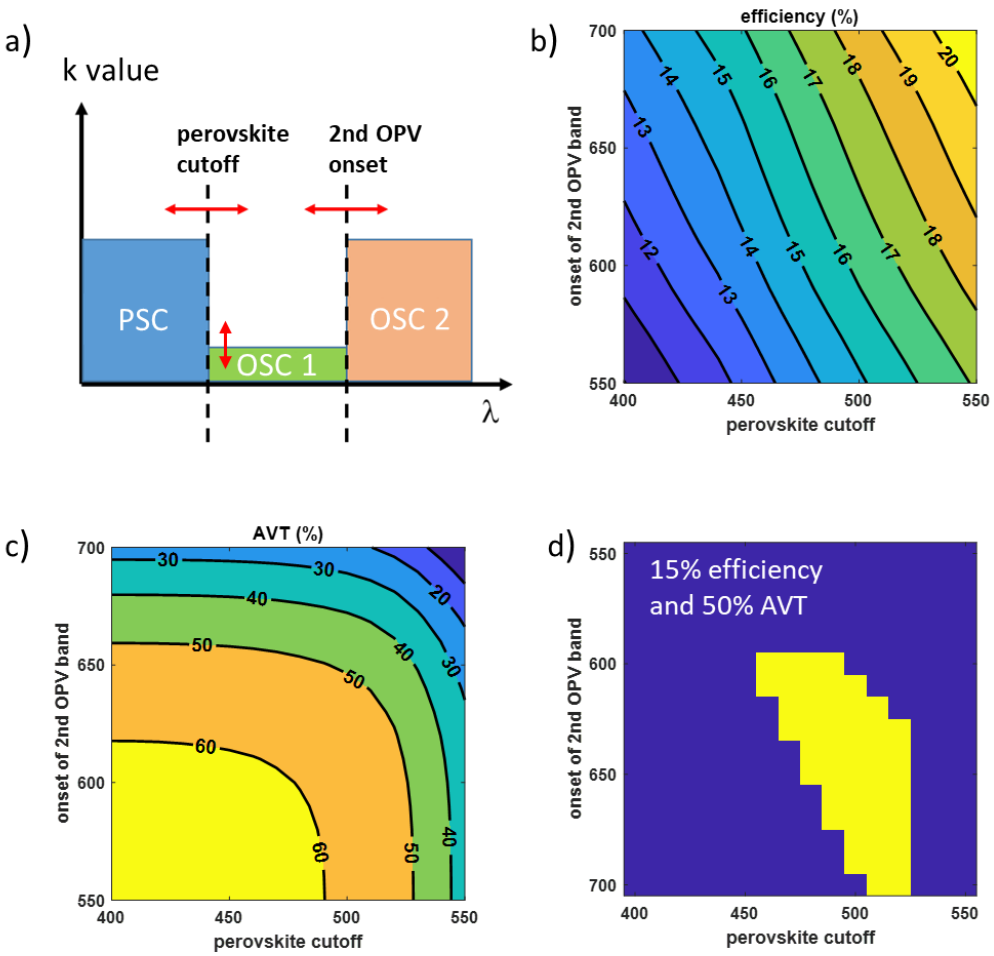

Figure 1: Results of basic simulations performed to assess the influence of the absorption spectra of PSC and OSC absorber. a) Illustration of the assumed spectra with perovskite cutoff and onset of the second OPV band as variable parameters, b), c) efficiency and AVT depending on these paramters, d) binary plot (yellow = true, blue = false) indicating if exemplary values of 15 % efficiency and 50 % AVT are achieved. The terms 'onset' and 'cutoff' are used with respect to wavelength as indicated.

These results highlight that the choice of high and low bandgap absorbers represents the crucial point of the whole workflow.

Considering the feasibility study described above, we investigated the possibility of achieving similar efficiencies (>15%) and AVT (> 50%) by simulating TPV PSC-OSC tandems with realistic materials and considering several connection schemes between the top and bottom cells. We designed the top-cell based on high bandgap methylammonium lead bromide/chloride perovskite ($MAPbBr_{3-x}Cl_x$). This class of perovskites exhibits a variable bandgap of 1.57-3 eV and power conversion efficiencies ranging from 0.5% [6] up to 10.4% [13], depending on the composition, and is therefore suitable for UV-selective absorption. For the low bandgap bottom cell design we opted for an OSC based on PTB7-Th:IEICO-4F bulk-heterojunction system capable to reach PCEs up to 10% at 40% AVT [14].

The use of an ultra-narrow band gap non-fullerene acceptor such as the IEICO-4F allows to have a strong NIR-selective absorption. As depicted in **Figure 2a**, the UV selective absorption of perovskite (500-540 nm with $0 \leq x \leq 0.78$) combined with the NIR selective absorbing blend (centered at 840 nm) limits the light-harvesting overlap in the visible range and opens the way to achieve high transparency.

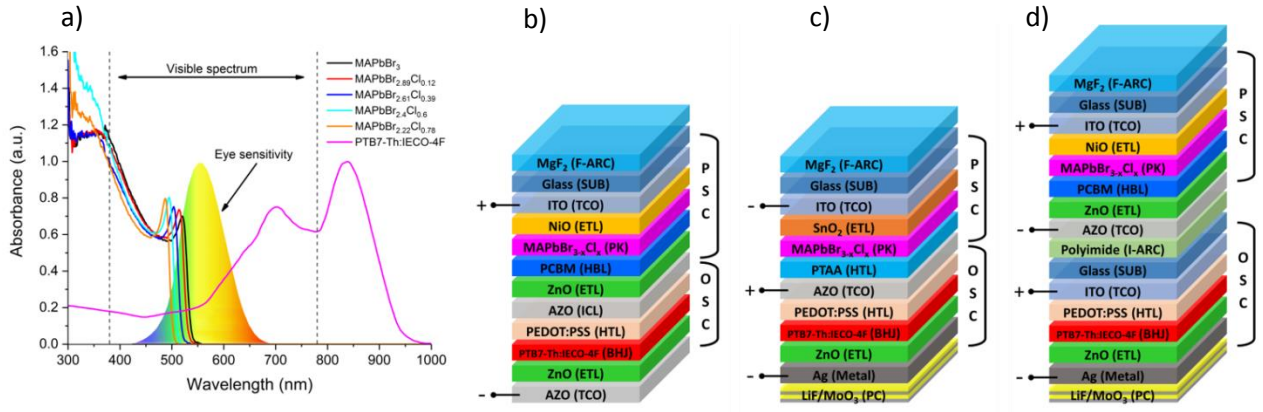

Figure 2: (a) Normalized absorption spectra measured for the $MAPbBr_{3-x}Cl_x$ perovskites and PTB7-Th:IEICO-4F blend compared with the human eye sensitivity function. Schematic structure of the (b) 2T, (c) 3T and (d) 4T tandem solar cells used for the electro-optical modeling, including the perovskite and bulk heterojunction absorbers (PK and OSC), hole and electron transport layers (HTL and ETL), transparent conductive oxides (TCO), anti-reflective coating (ARC), interconnecting layer (ICL), sealing material (Seal) and photonic crystals (PC).

We investigate the impact on efficiency and AVT of different design strategies that consider: i) bandgap tuning of the methylammonium lead bromide/chloride perovskite, ii) different tandem architectures, and iii) dimension and optimization of cell stack. For the latter we focus our attention on transparent electrodes, anti-reflective coatings (ARCs) and multilayer dielectric structures for light management.

We consider the three main architectures shown in **Figure 2(b-d)**, named as 2-Terminal (2T), 3-Terminal (3T) and 4-Terminal (4T), respectively. The difference between them is given by the number of terminals connected to the maximum power point tracker (MPPT) used to maximize the power extraction. While for the 4T tandem two individual MPPTs are required to maximize the operation of both the top and bottom cell, in the 2T architecture the top and bottom cells are monolithically connected in series configuration, therefore a single MPPT rules the global device

operation. For the 3T configuration, we can opt for one MPPT connecting the two cells in parallel, or two MPPT if the cells are treated independently. However, considering that the top and bottom cells have very different V_{oc} the two MPPTs configuration is preferred. In terms of performance, the monolithic integration in the 2T and 3T tandem favors the transparency due to the reduced number of transparent conductive oxide (TCO) layers required (respectively 2 and 3), while the 4T tandem obtained by mechanically stacking the top and bottom cell requires an intermediate layer for the anti-reflection and sealing. The 3T and 4T tandem architectures permit the maximization of power conversion since the overall efficiency is equivalent to the sum of top and bottom cell, while in the 2T tandem it is limited by the required current matching condition [8], [15]. Despite the fact that the sub-cells contribute separately to the overall PCE in the 3T tandem, the difficulties in the design of interconnections make this configuration more challenging [16].

Considering these limitations and requirements, the design proceeds with a step-by-step optimization starting from the choice of transparent electrodes, followed by the single cells up to the final configuration. In order to explore all the three aforementioned tandem architectures, we investigate both the direct (N-I-P) and inverted (P-I-N) planar PSC architectures that allow us to guarantee the proper connection of terminals. In all the simulation we will consider ITO coated glass substrates as they allow the highest device transparency due to the reduction of optical losses [17]–[19], which is shown by comparing ITO and fluorine-doped tin oxide (FTO) (see **Figure S2**).

Semi-transparent perovskite solar cells

The evaluation of performance achievable with PSC is performed by taking into account both the direct and inverted planar architectures for the design of the top cell within 2T, 3T and 4T tandem structures. For the perovskite stack, we considered the following architectures:

- Direct (N-I-P): Glass/ITO or FTO/ETL/$MAPbBr_3$/PTAA/AZO as N-I-P;

- Inverted (P-I-N): Glass/ITO/HTL/$MAPbBr_3$/PCBM/ZnO/AZO as P-I-N.

For the direct structure, we fixed poly(triaryl)amine (PTAA) as hole transport layer (HTL), while for the indirect we fixed (6,6)-Phenyl-C61-Butyric Acid Methyl Ester (PCBM) and zinc oxide (ZnO) [8][20] as electron blocking layer (EBL) and electron transport layer (ETL), respectively. For the transparent back electrode, we consider only aluminum doped zinc oxide (ZnO:Al or AZO) since it exhibits suitable features like tunable work function (WF), low sheet resistance and high transparency in the visible and NIR range, [21] which are very suited for the tandem architecture we are studying. Regarding the top transparent electrode which includes the glass substrate, we consider both optimized ITO and FTO for the direct architecture and only the optimized ITO for the inverted architecture.

A preliminary screening of solar cell performances achievable for $MAPbBr_3$ and for several choices of the other transporting layers has been performed via optical calculations considering the refractive indexes and the extinction coefficient reported in **Figures S3** and **S4**. By varying the thickness of $MAPbBr_3$ and the transporting layers we obtain a map (**Figure S5**) for AVT and J_{sc} (see SI). For the n-i-p architecture we consider both tin oxide (SnO_2) or titanium dioxide (TiO_2) as ETL and FTO or ITO as transparent conductive electrodes (see **Figures S5a-c**). For the p-i-n architecture we considered nickel oxide (NiO), poly(3,4-ethylenedioxythiophene) polystyrene sulfonate (PEDOT:PSS) and PTAA as possible alternatives for HTL (**Figures S5d-f**) [22]. The results show that the use of ITO/SnO_2 for the direct n-i-p structure (**Figure S5a)** and ITO/NiO for the indirect p-i-n structure (**Figure S5d)** permit the best trade-off between photoconversion and AVT.

These two most performant structures were further investigated through electro-optical simulations. TMM calculations are performed to determine the AVT and generation profile, while JV characteristics and consequently all the photovoltaic parameters are determined by performing DD simulations.

The inverted and direct PSC stack simulated were modelled by using the energy levels as depicted in **Figure 3(a,c)** and electrical parameters reported in **Table S1**.

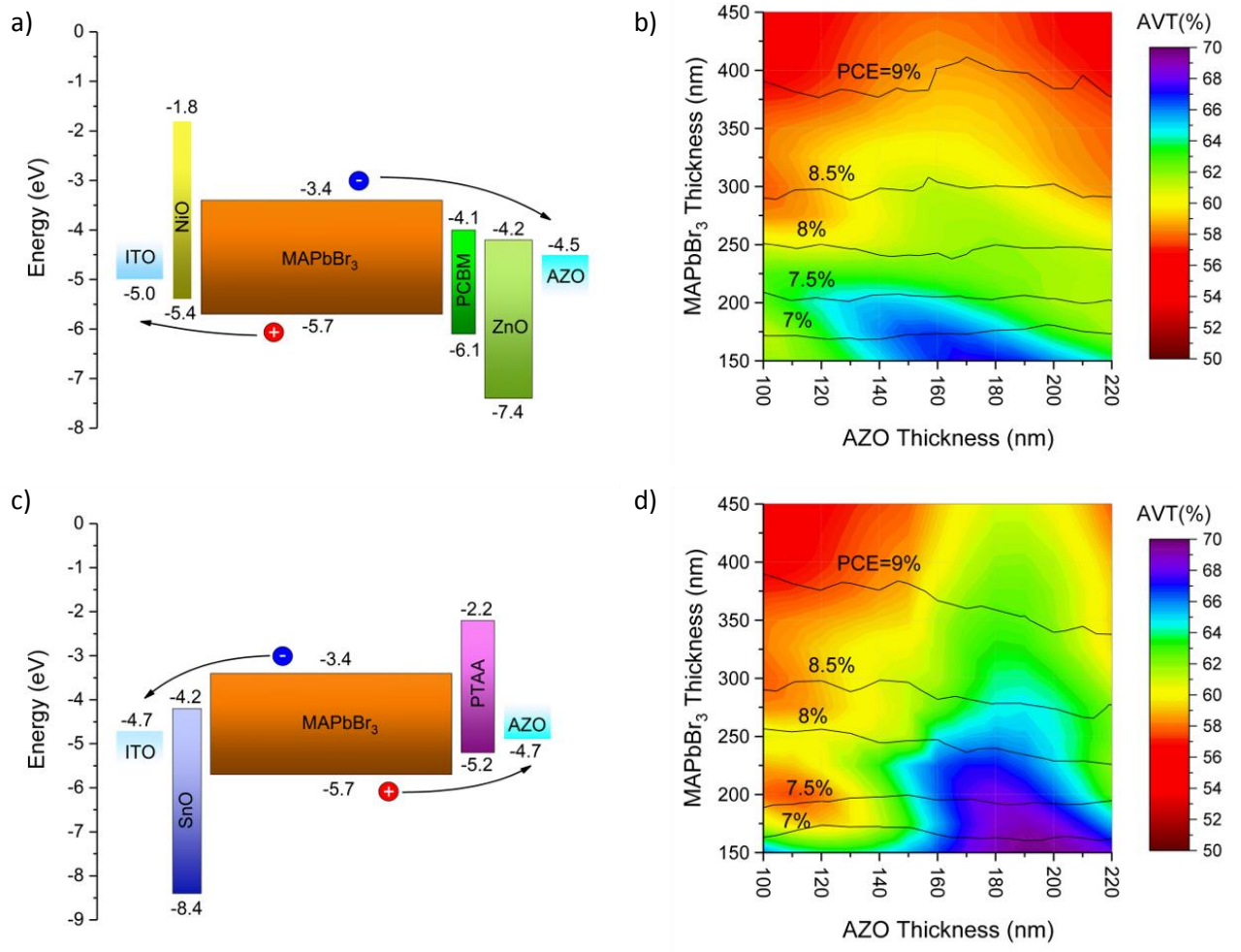

Figure 3: (a, c) Band alignments and (b, d) 2D color maps indicating the AVT and PCE calculated with electro-optical simulations for the P-I-N and N-I-P planar architectures by varying the $MAPbBr_3$ and AZO thickness. The thickness of each transport and blocking layer of the structures is considered constant for all calculations and is set in order to limit the optical losses but keeping efficient charge carrier extraction (10 nm-thick NiO_2, 15 nm-thick $PC_{60}BM$, 50 nm-thick ZnO, 20 nm-thick SnO_2 and 25nm-thick PTAA).

Figure 3b and 3d display the obtained 2D color maps representing the AVT achieved for the inverted and direct PSCs, respectively, and the corresponding PCE indicated by contour lines. The results show that although both configurations allow to achieve PCE values of around 9.3-9.4% in the range of thicknesses explored, the n-i-p structure exhibits a larger AVT (61.4% for a PCE of 9.34%) compared to the p-i-n structure (AVT=58% at PCE of 9.31%).

Semi-transparent organic solar cells

In order to design the bottom cell, we evaluated the performance of the selectively absorbing NIR OSC composed by the following stack: Glass/ITO/PEDOT:PSS/PTB7-Th:IEICO-4F/ZnO/Back-electrode. In particular, we investigated and compared the electro-optical performance achievable by adopting either a transparent conductive oxide (AZO) or a very thin silver layer coated by a one-dimensional photonic crystal (PC) as back-electrode [14], [23].

Electro-optical simulations are performed by using the optimized Glass(0.7 mm)/ITO(142 nm) substrate as front electrode (see **Figure S2a**), 40 nm-thick PEDOT:PSS (HTL) [14] and 50 nm-thick ZnO (ETL). The thickness of both transport layers is the same in all simulations and is chosen to guarantee a good carrier extraction at both contacts.

The light management through the use of photonic crystals is aimed to provide a selective back-reflection for the NIR component centered at the Bulk HeteroJunction (BHJ) PTB7-Th:IEICO-4F absorption peak (840 nm), thus increasing its absorption by the OSC, without compromising the transparency in visible range. Here again, preliminary optical calculations have been performed in order to determine the most effective design of PC giving the best trade-off between photoconversion and AVT. We considered and compared a conventional Distributed Bragg Reflector (DBR) made by a molybdenum trioxide (MoO_3)/ lithium fluoride (LiF) multilayer [24] and a specific PC structure based on alternating LiF and MoO_3 [14].

The result of this optimization process (**Figures S6** and **S7)** shows that the PC structure based on Ag(20 nm)/LiF(165 nm)/MoO_3(65 nm)/LiF(95 nm)/MoO_3(120 nm) has to be preferred over a DBR and the thin Ag contact (20 nm). In fact, the use of a PC on the Ag thin layer allows to increase both the AVT (of 20-22%) and photocurrent density (of 0.1-0.25 mA/cm^2) for a BHJ with thicknesses up to 60 nm. For BHJ thicker than 60 nm the PC only influences the AVT (increase of 15-19%) while the absorption remains practically unchanged.

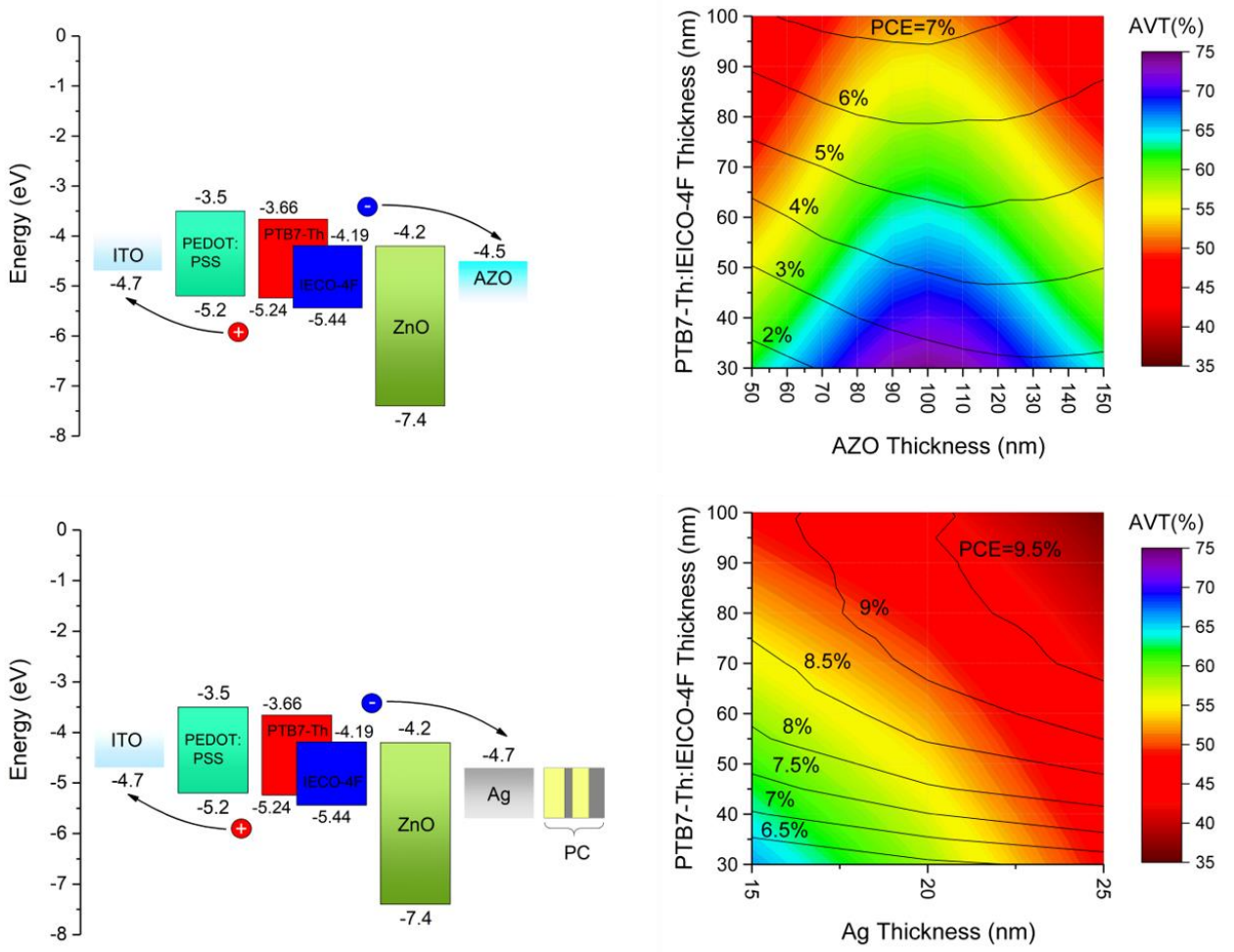

Figure 4: (a, c) Band alignments and (b, d) 2D color maps indicating the AVT and PCE calculated with electro-optical simulations for the OSC by varying the PTB7-Th:IEICO-4F and back electrode (AZO and Ag) thickness. Photonic crystal are composed by the following stack: LiF(165 nm)/MoO_3(65 nm)/LiF(95 nm)/MoO_3(120 nm).

Electro-optical simulations comparing OSCs with AZO and PC electrodes have been performed by considering the energy level alignments reported in **Figure 4(a,c)** and the electrical parameters given in **Table S2.** For the OSC, in both TMM and DD simulations the BHJ layer made by PTB7-Th:IEICO-4F is considered as an effective material, therefore it is modelled by using global optical constants (**Figure S3**) and effective acceptor-donor energy levels, such as LUMO=-4.19 eV HOMO=-5.24 eV [25]. Simulation results are shown in the 2D color maps of **Figure 4b** and **Figure 4d** for AZO and PC based OSCs, respectively. The importance of light management is clearly demonstrated owing to its beneficial effect on the PCE: for AVT=50% the PCE increases from 7.8% for the AZO electrode to 10.3% when the Ag/PC is used. On the other hand, the results highlight that

the thickness of the Ag layer is quite crucial, since a drop of AVT occurs for thick Ag. Therefore, by evaluating the electrical and optical requirements we selected a 20 nm-thick Ag [14], which ensures at same time low sheet resistance of 1-5 Ω/□ [20] and good transparency, showing AVT of 43-58%. The use of a transparent back electrode, instead, has a strong impact on the transparency, in fact a 100 nm-thick AZO allows to have a gain of up to 20% on AVT.

Semi-transparent tandem solar cells

2T, 3T and 4T tandem solar cells are designed by combining the individual semi-transparent PSCs and OSCs as described and optimized in the previous sections. As shown in **Figure 2(b-d)**, the P-I-N PSC is used as top cell in the 2T and 4T, while the N-I-P PSC is used in the 3T since here the p-type terminal is in common [16]. The PCE of the tandem cell is maximized in order to preserve the AVT around 50%, using an optimization process that can be summarized in the following steps: i) combine the top and bottom cell as individually designed, ii) tune of top cell bandgap by varying the chlorine content of the $MAPbBr_{3-x}Cl_x$ perovskite, iii) evaluation of the use of photonic crystals in the NIR selective OSC to improve the performance, and iv) find the best thickness for materials constituting the front and intermediate anti-reflection coating (F-ARC and I-ARC, respectively) as introduced in **Figure S8** and **Figure S9**).

The 2D color maps in **Figure 5(a-c)** show the results of the optimization process obtained for the three tandem configurations investigated. These maps provide a full overview of the electro-optical performance achievable for the three configurations as a function of the thickness of the top and bottom absorbers.

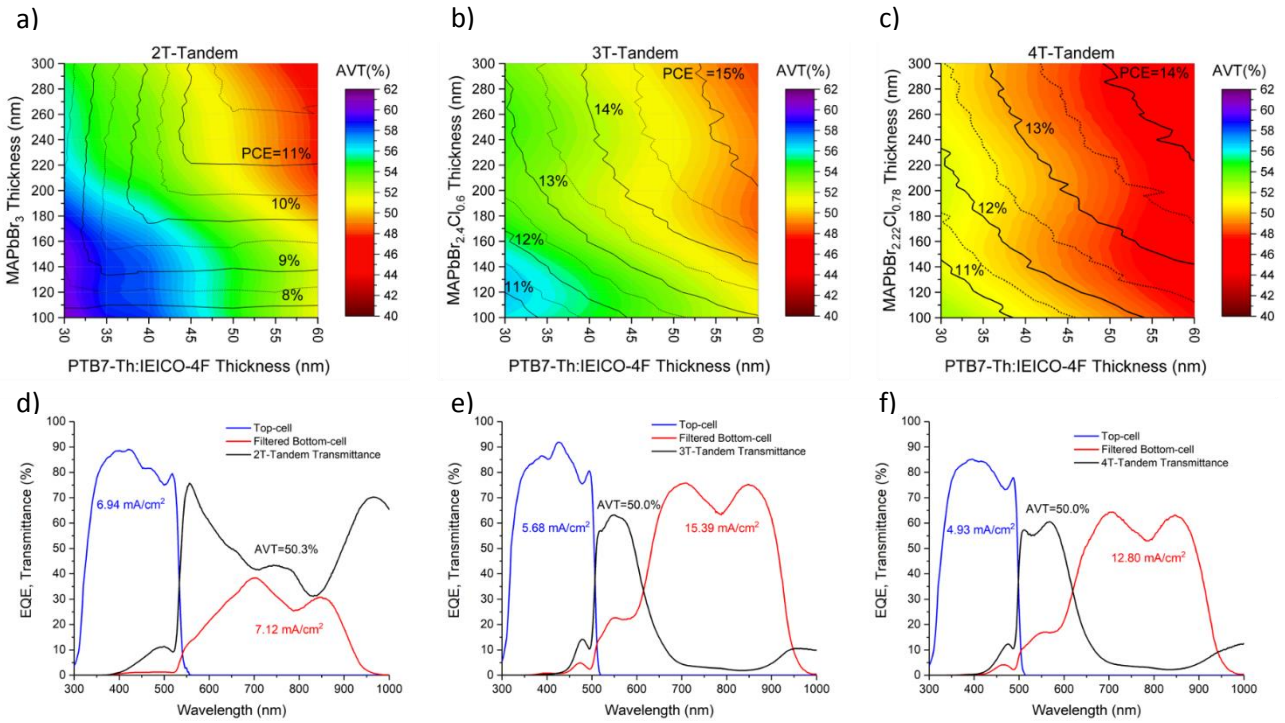

Figure 5: (a-c) 2D color maps indicating the AVT vs. $MAPbBr_{3-x}Cl_x$ and PTB7-Th:IEICO-4F thickness which summarize the results obtained on the 2T, 3T and 4T tandem devices. The black level curves included in plots indicate the PCE achievable depending on the individual thickness of absorbers. (d-f) External quantum efficiency (EQE) of the top (blue) and bottom (red) cell of the different tandem configurations including the integrated current density; the transmittance (black) is used to evaluate the global AVT.

The 2T tandem is the only one for which the perovskite bandgap tuning and photonic crystals are not required since AVT > 50% can be achieved (**Figure S10a**) by using $MAPbBr_3$ and a transparent back electrode. This is due to the limited number of TCOs needed, and to the fact that the current matching is already achieved without increasing the NIR absorption. Thus, the use of only AZO as final transparent electrode represents a benefit for the global AVT of a 2T tandem (**Figure S10b**). In particular, when the PC is added to the bottom cell, replacing the AZO electrode, the increase of PCE is accompanied by a dramatic drop of the AVT (**Figure S10c**).

Differently, the 3T and 4T tandem architectures need a bandgap tuning optimization step. For this purpose electro-optical simulations are performed by varying the Cl content of the $MAPbBr_{3-x}Cl_x$ x=0.12, 0.39, 0.6 and 0.78, shifting the energy of the absorption edge of the top cell to higher energies with a consequent increase of the AVT. Optical constants used in TMM calculations and electrical parameters used in DD simulations are reported in **Figure S3** and **Table S3**, respectively.

All architectures have been further optimized by considering a frontal anti-reflecting coating of magnesium fluoride (MgF_2), which is widely used in TPV applications [26][27] since it exhibits

intermediate refractive index between the air and glass substrate (**Figure S8a**). Its optimal thickness is calculated for each architecture in order to reduce the optical losses by reflection at the top interface between the air and the glass substrate. The results obtained from optical calculations show that the optimal frontal ARC is slightly different depending on the terminal configuration. Indeed, both the PCE and AVT where optimized by using a front ARC (F-ARC) thickness of 105, 95 and 100 nm for the 2T, 3T and 4T tandem cell, respectively (**Figure S9(a-c)**).

An additional intermediate ARC (I-ARC) is applied to the 4T tandem, whose structure is the only one based on the mechanical integration of the top and bottom cell, thus the I-ARC should work as adhesive layer. Polyimide (PI) represents the ideal candidate thanks to a refractive index compatible with the AZO/Glass interfaces (**Figure S8b**), low absorption in visible range [28], low temperature processability and its adhesive properties. This makes PI suitable for fully inorganic tandem solar cell devices [29][30]. Simulations results reported in the 2D color map of **Figure S9d** show that a 80 nm-thick polyimide layer can be successfully included in the 4T tandem architecture to improve the PCE and AVT performance. Notably, a detailed overview of intermediate and final results obtained on the 2T, 3T and 4T solar cells is summarized in **Figure S10, S11** and **S12**. In each color map reported in the Supplementary Information we show the impact on AVT and PCE of the: ii) $MAPbBr_{3-x}Cl_x$ bandgap tuning, iii) photonic crystals, iv) frontal and intermediate anti-reflective coating.

The design workflow, as described, allowed to explore several combinations in terms of thickness and composition between the perovskite and bulk-heterojunction based absorbers, in the range of 100-300 nm and 30-60 nm, respectively. The stack design of the most performant tandem solar cells having AVT = 50% are summarized in **Table 1**.

Table 1: Dimension of each layer for the best performing tandem solar cell stacks showing AVT=50% obtained for the 3 different architectures (2T, 3T and 4T).

Device	Cell	ARC	Substrate	TL	Absorber	EBL	TL	Contact	PC
2T	PSC	MgF_2 105 nm	Glass/SiO_2/ITO 0.7mm/20nm/142nm	NiO 10 nm	$MAPbBr_3$ 275 nm	$PC_{60}BM$ 15 nm	ZnO 50 nm	AZO 190 nm	- -
	OSC	- -	- -	PEDOT:PSS 40 nm	PTB7-Th:IEICO-4F 50 nm	- -	ZnO 50 nm	AZO 110 nm	- -
3T	PSC	MgF_2 95 nm	Glass/SiO_2/ITO 0.7mm/20nm/142nm	SnO_2 20 nm	$MAPbBr_{2.4}Cl_{0.6}$ 240 nm	- -	PTAA 25 nm	AZO 180 nm	- -
	OSC	- -	- -	PEDOT:PSS 40 nm	PTB7-Th:IEICO-4F 55 nm	- -	ZnO 50 nm	Ag 20 nm	LiF/MoO_3 2 pairs
4T	PSC	MgF_2 100 nm	Glass/SiO_2/ITO 0.7mm/20nm/142nm	NiO 10 nm	$MAPbBr_{2.22}Cl_{0.78}$ 225 nm	$PC_{60}BM$ 15 nm	ZnO 50 nm	AZO 110 nm	- -
	OSC	Polyimide 80 nm	Glass/SiO_2/ITO 0.7mm/20nm/142nm	PEDOT:PSS 40 nm	PTB7-Th:IEICO-4F 40 nm	- -	ZnO 50 nm	Ag 20 nm	LiF/MoO_3 2 pairs

In addition, for these stacks we show in **Figure 5(d-f)** the individual external quantum efficiency (EQE) obtained for the top (blue) and bottom (red) cell, and the overall transmittance (black) in the investigated range of wavelength of 300-1000 nm. The tandem cell transmittance takes different shapes depending on terminal layout and perovskite composition. In fact, unlike in the 3T and 4T tandem, the current matching condition in 2T affects the balance between the UV and NIR absorption with a larger transmittance in the red part of the spectrum compared to the 3T and 4T configurations.

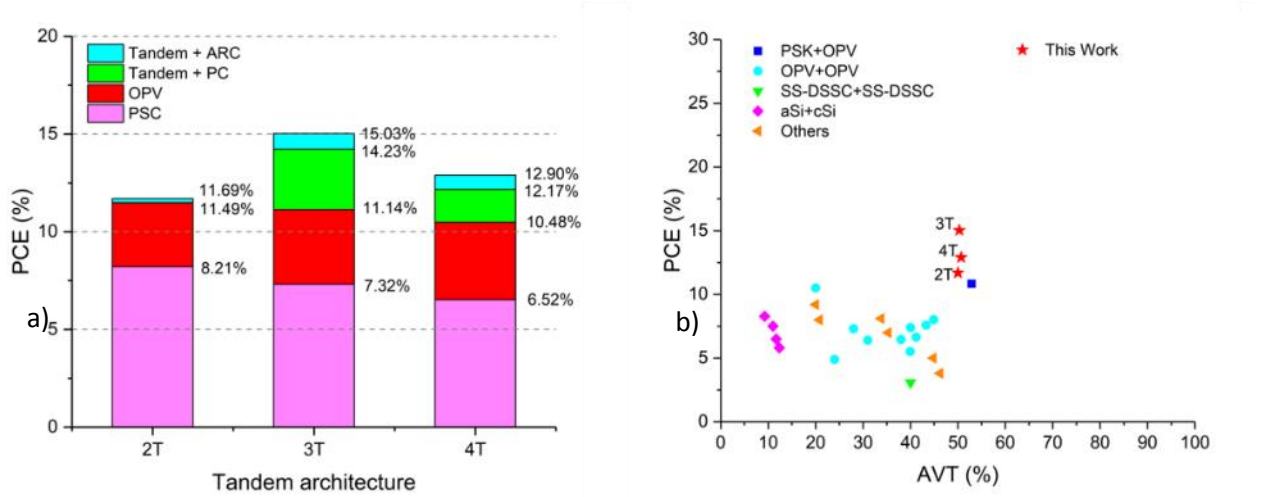

Figure 6: (a) Summary of simulations results showing the performance achievable for the different terminals configuration of tandem devices including splitting contributions to the overall given by: the top cell, bottom cell, photonic crystals and anti-reflecting coatings. (b) Efficiency vs. the AVT of the published and theoretical results obtained in this work.

The JV characteristics of the best performing stack for each tandem configuration as obtained with DD simulations is reported in **Figure S13 (a-c)**. The PCEs of the tandem cells with AVT of 50% are summarized in **Figure 6a** where we also indicate the contribution to the efficiency for each

component of the cell, namely PSC, OSC, PC and ARC. PCEs of 11.69%, 15.03% and 12.9% can be achieved for the 2T, 3T and 4T tandem architecture, respectively. For the 2T configuration the theoretical result of 11.69% is in good agreement with the experimental value of 10.7% [8]. These results show that the current record efficiency for transparent PV can be improved by more than 50% by a proper choice of the architecture (**Figure 6b**).

The bar plots in **Figure 6a** show that the best design strategy allowing to maximize the performance and transparency varies depending on the number and configuration of terminals. The current matching condition imposed by the series connection of the 2T architecture limits the optimization of the PCE and AVT, and therefore the absorption in the perovskite based top cell represents the bottleneck. In fact, a shift of the absorption edge to higher energies increases the AVT, but at the same time it reduces the photocurrent in the tandem device, thus affecting the global PCE. For the same reasons, the use of frontal anti-reflective coating aimed at reducing the optical losses provides some improvement but is not crucial, as demonstrated by the modest increase of only +0.2% on the global PCE. Results obtained for 3T and 4T architectures suggest a different design strategy based on the interplay between perovskite bandgap tuning and light management. The reduced absorption in the UV by shifting the perovskite absorption edge to higher energy can be compensated by the increase of the absorption in the NIR range thanks to the one-dimensional photonic crystal. The lower PCE of the 3T and 4T tandems before optimization compared to the 2T tandem is easily overcome when the PC is added, leading to a substantial increase in PCE of +2.09% and +1.69%, respectively. Therefore, the use of a PC in these structures has a high impact on the performance and represents the crucial step capable of pushing this technology beyond the current state of the art.

The color appearance of the designed tandem solar cells are summarized in the CIE xy chromaticity diagram of **Figure S13d**, including aesthetical implications such as the color rendering index (CRI) and correlated color temperature (CCT) [31] (see also **Figure S14** and discussion therein). The difference in the UV-NIR selective absorption coming from the architecture affects the neutrality,

brightness and perception of transmitted light. The 2T tandem shows a CRI = 62.6%, which is 7% and 12% more than the 4T and 3T, respectively. In terms of color temperature, the 2T tandem has a CCT of 3405 K, while the 3T and 4T cells exhibit higher CCT of 4442 K and 4467 K, respectively.

Conclusions

In this work, we have presented electro-optical simulations for the design of highly efficient semi-transparent Perovskite/Organic tandem solar cells using a combined UV and NIR selective absorption approach. Initial simulations with hypothetic rectangular absorption spectra highlight the requirement of choosing absorbers with optimized absorption spectra to achieve high PCE and high AVT at the same time. The investigation of the 2T, 3T and 4T architectures for the realization of tandem cells provided a full overview over the potential of methylammonium lead mixed bromide-chloride perovskite ($MAPbBr_{3-x}Cl_x$) and non-fullerene based bulk heterojunction (PTB7-Th:IEICO-4F) absorbers. The investigation allowed to extract important guidelines in terms of: stack dimensioning, use of frontal and intermediate anti-reflective coating and impact of the light management on performance by using one-dimensional photonic crystals.

The results obtained clearly show that the current record efficiency of 10.7% for semi-transparent tandem technology can be improved with all the three architectures proposed, and that a breakthrough PCE of ≈15% can be achieved while guaranteeing an AVT = 50%, thus making this PSC/OSC tandem approach very appealing for BIPV applications.

Acknowledgements

This project has received funding from the European Union's Horizon 2020 research innovation programme under grant agreement No. 101007084 (CITYSOLAR).

References

[1] C. J. Traverse, R. Pandey, M. C. Barr, and R. R. Lunt, "Emergence of highly transparent photovoltaics for distributed applications," *Nat. Energy*, vol. 2, no. 11, pp. 849–860, Nov. 2017, doi: 10.1038/s41560-017-0016-9.

[2] W. Wang *et al.*, "Fused Hexacyclic Nonfullerene Acceptor with Strong Near-Infrared Absorption for Semitransparent Organic Solar Cells with 9.77% Efficiency," *Adv. Mater.*, vol. 29, no. 31, p. 1701308, Aug. 2017, doi: 10.1002/adma.201701308.

[3] Y. Song, S. Chang, S. Gradecak, and J. Kong, "Visibly-Transparent Organic Solar Cells on Flexible Substrates with All-Graphene Electrodes," *Adv. Energy Mater.*, vol. 6, no. 20, p. 1600847, Oct. 2016, doi: 10.1002/aenm.201600847.

[4] C.-Y. Chang *et al.*, "Highly Efficient Polymer Tandem Cells and Semitransparent Cells for Solar Energy," *Adv. Energy Mater.*, vol. 4, no. 7, p. 1301645, May 2014, doi: 10.1002/aenm.201301645.

[5] Z. Tang *et al.*, "Semi-Transparent Tandem Organic Solar Cells with 90% Internal Quantum Efficiency," *Adv. Energy Mater.*, vol. 2, no. 12, pp. 1467–1476, Dec. 2012, doi: 10.1002/aenm.201200204.

[6] D. Liu, C. Yang, and R. R. Lunt, "Halide Perovskites for Selective Ultraviolet-Harvesting Transparent Photovoltaics," *Joule*, vol. 2, no. 9, pp. 1827–1837, Sep. 2018, doi: 10.1016/j.joule.2018.06.004;

[7] Q. Liu *et al.*, "Light Harvesting at Oblique Incidence Decoupled from Transmission in Organic Solar Cells Exhibiting 9.8% Efficiency and 50% Visible Light Transparency," *Adv. Energy Mater.*, vol. 10, no. 17, p. 1904196, May 2020, doi: 10.1002/aenm.201904196.

[8] L. Zuo, X. Shi, W. Fu, and A. K. - Y. Jen, "Highly Efficient Semitransparent Solar Cells with Selective Absorption and Tandem Architecture," *Adv. Mater.*, vol. 31, no. 36, p. 1901683, Sep. 2019, doi: 10.1002/adma.201901683.

[9] Y.-F. Chiang, R.-T. Chen, A. Burke, U. Bach, P. Chen, and T.-F. Guo, "Non-color distortion for visible light transmitted tandem solid state dye-sensitized solar cells," *Renew. Energy*, vol. 59, pp. 136–140, Nov. 2013, doi: 10.1016/j.renene.2013.03.018.

[10] A. R. bin M. Yusoff, S. J. Lee, F. K. Shneider, W. J. da Silva, and J. Jang, "High-Performance Semitransparent Tandem Solar Cell of 8.02% Conversion Efficiency with Solution-Processed Graphene Mesh and Laminated Ag Nanowire Top Electrodes," *Adv. Energy Mater.*, vol. 4, no. 12, p. 1301989, Aug. 2014, doi: 10.1002/aenm.201301989.

[11] M. C. Troparevsky, A. S. Sabau, A. R. Lupini, and Z. Zhang, "Transfer-matrix formalism for the calculation of optical response in multilayer systems: from coherent to incoherent interference," *Opt. Express*, vol. 18, no. 24, p. 24715, Nov. 2010, doi: 10.1364/OE.18.024715.

[12] M. Auf der Maur, G. Penazzi, G. Romano, F. Sacconi, A. Pecchia, and A. Di Carlo, "The Multiscale Paradigm in Electronic Device Simulation," *IEEE Trans. Electron Devices*, vol. 58, no. 5, pp. 1425–1432, May 2011, doi: 10.1109/TED.2011.2114666.

[13] J. H. Heo, D. H. Song, and S. H. Im, "Planar CH 3 NH 3 PbBr 3 Hybrid Solar Cells with 10.4% Power Conversion Efficiency, Fabricated by Controlled Crystallization in the Spin-Coating Process," *Adv. Mater.*, vol. 26, no. 48, pp. 8179–8183, Dec. 2014, doi: 10.1002/adma.201403140.

[14] R. Xia, C. J. Brabec, H.-L. Yip, and Y. Cao, "High-Throughput Optical Screening for Efficient Semitransparent Organic Solar Cells," *Joule*, vol. 3, no. 9, pp. 2241–2254, Sep. 2019, doi: 10.1016/j.joule.2019.06.016.

[15] J. Werner, B. Niesen, and C. Ballif, "Perovskite/Silicon Tandem Solar Cells: Marriage of Convenience or True Love Story? – An Overview," *Adv. Mater. Interfaces*, vol. 5, no. 1, p. 1700731,

Jan. 2018, doi: 10.1002/admi.201700731.

[16] T. Todorov, O. Gunawan, and S. Guha, “A road towards 25% efficiency and beyond: perovskite tandem solar cells,” *Mol. Syst. Des. Eng.*, vol. 1, no. 4, pp. 370–376, 2016, doi: 10.1039/C6ME00041J.

[17] L. Scholtz, L. Ladanyi, and J. Mullerova, “Influence of Surface Roughness on Optical Characteristics of Multilayer Solar Cells,” *Adv. Electr. Electron. Eng.*, vol. 12, no. 6, Jan. 2015, doi: 10.15598/aeee.v12i6.1078.

[18] A. Way *et al.*, “Fluorine doped tin oxide as an alternative of indium tin oxide for bottom electrode of semi-transparent organic photovoltaic devices,” *AIP Adv.*, vol. 9, no. 8, p. 085220, Aug. 2019, doi: 10.1063/1.5104333.

[19] L. Olteanu, R. M. Ion, I. A. Bucurică, I. V. Gurgu, I. D. Dulamă, and S. Teodorescu, “ITO AND FTO COATED GLASS CHARACTERIZATION USING SEM AND AFM TECHNIQUES,” *Bull. Transilv. Univ. Brasov. Ser. I - Eng. Sci.*, vol. 12(61), no. 2, pp. 41–46, Feb. 2020, doi: 10.31926/but.ens.2019.12.61.1.15.

[20] D. Liu *et al.*, “Improved performance of inverted planar perovskite solar cells with F4-TCNQ doped PEDOT:PSS hole transport layers,” *J. Mater. Chem. A*, vol. 5, no. 12, pp. 5701–5708, 2017, doi: 10.1039/C6TA10212C.

[21] X. Yu, X. Yu, J. Zhang, D. Zhang, H. Cai, and Y. Zhao, “Interfacial modification for improving inverted organic solar cells by poly(N-vinylpyrrolidone),” *RSC Adv.*, vol. 5, no. 73, pp. 58966–58972, 2015, doi: 10.1039/C5RA09427E.

[22] X. Yin *et al.*, “Highly Efficient Flexible Perovskite Solar Cells Using Solution-Derived NiO x Hole Contacts,” *ACS Nano*, vol. 10, no. 3, pp. 3630–3636, Mar. 2016, doi: 10.1021/acsnano.5b08135.

[23] W. Yu *et al.*, “Semitransparent polymer solar cells with one-dimensional (WO 3 /LiF) N photonic crystals,” *Appl. Phys. Lett.*, vol. 101, no. 15, p. 153307, Oct. 2012, doi: 10.1063/1.4760229.

[24] Q. Ou, Y. Li, and J. Tang, “Light Manipulation in Organic Photovoltaics,” *Adv. Sci.*, vol. 3, no. 7, p. 1600123, Jul. 2016, doi: 10.1002/advs.201600123.

[25] X. Song *et al.*, “Controlling Blend Morphology for Ultrahigh Current Density in Nonfullerene Acceptor-Based Organic Solar Cells,” *ACS Energy Lett.*, vol. 3, no. 3, pp. 669–676, Mar. 2018, doi: 10.1021/acsenergylett.7b01266.

[26] Y. Li *et al.*, “Color-neutral, semitransparent organic photovoltaics for power window applications,” *Proc. Natl. Acad. Sci.*, vol. 117, no. 35, pp. 21147–21154, Sep. 2020, doi: 10.1073/pnas.2007799117.

[27] A. J. Bett *et al.*, “Semi-Transparent Perovskite Solar Cells with ITO Directly Sputtered on Spiro-OMeTAD for Tandem Applications,” *ACS Appl. Mater. Interfaces*, vol. 11, no. 49, pp. 45796–45804, Dec. 2019, doi: 10.1021/acsami.9b17241.

[28] M. Campoy-Quiles, J. Nelson, D. D. C. Bradley, and P. G. Etchegoin, “Dimensionality of electronic excitations in organic semiconductors: A dielectric function approach,” *Phys. Rev. B*, vol. 76, no. 23, p. 235206, Dec. 2007, doi: 10.1103/PhysRevB.76.235206.

[29] I. Mathews, D. O’Mahony, K. Thomas, E. Pelucchi, B. Corbett, and A. P. Morrison, “Adhesive bonding for mechanically stacked solar cells,” *Prog. Photovoltaics Res. Appl.*, vol. 23, no. 9, pp. 1080–1090, Sep. 2015, doi: 10.1002/pip.2517.

[30] T. Sameshima *et al.*, “Multi Junction Solar Cells Stacked with Transparent and Conductive Adhesive,” *Jpn. J. Appl. Phys.*, vol. 50, no. 5, p. 052301, May 2011, doi: 10.1143/JJAP.50.052301.

[31] A. R. Robertson, “Computation of Correlated Color Temperature and Distribution Temperature,” *J. Opt. Soc. Am.*, vol. 58, no. 11, p. 1528, Nov. 1968, doi: 10.1364/JOSA.58.001528.

SUPPORTING INFORMATION

Design of highly efficient semi-transparent perovskite/organic tandem solar cells

Daniele Rossi[1], Karen Forberich[2,3], Fabio Matteocci[1], Matthias Auf der Maur[1], Hans-Joachim Egelhaaf[2,3], Christoph Brabec[2,3] and Aldo Di Carlo[1,3,*]

[1]CHOSE (Centre for Hybrid and Organic Solar Energy), Department of Electronic Engineering, University of Rome "Tor Vergata", 00133, Rome, Italy

[2]Forschungszentrum Jülich GmbH, Helmholtz-Institut Erlangen-Nürnberg für Erneuerbare Energien (IEK-11) Abteilung Hochdurchsatzmethoden in der Photovoltaik (ZAE-Kooperation) Immerwahrstr. 2, 91058 Erlangen

[3]Institute of Materials for Electronics and Energy Technology (i-MEET), Friedrich-Alexander Universität Erlangen-Nürnberg (FAU) Martensstraße 7, Erlangen, D-91058, Germany.

[4]National Research Council (CNR), Institute of Structure of Matter (ISM), 00133, Rome, Italy

[*]Corresponding Author: aldo.dicarlo@uniroma2.it

Initial simulations

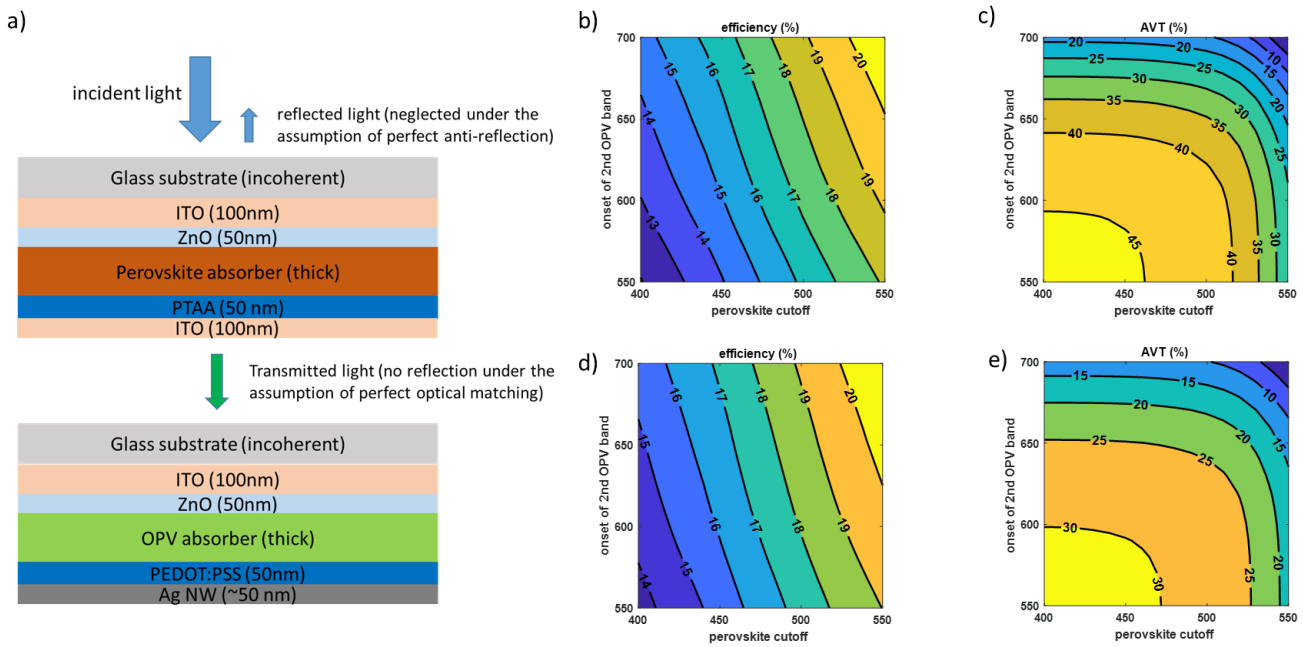

Figure S1: a) Stack used for the initial simulations with idealized rectangular absorption spectra. b,c): Efficiency and AVT obtained for ~30% absorption in the first OSC band, d),e): Efficiency and AVT obtained for ~50% absorption in the first OSC band.

Figure *S1* shows the stack used for the simulation results from Figure 1 in the main manuscript, and also efficiencies and AVT obtained for higher absorption (30% and 50%) in the second OSC band.

Sheet Resistance of commercial glass/TCO

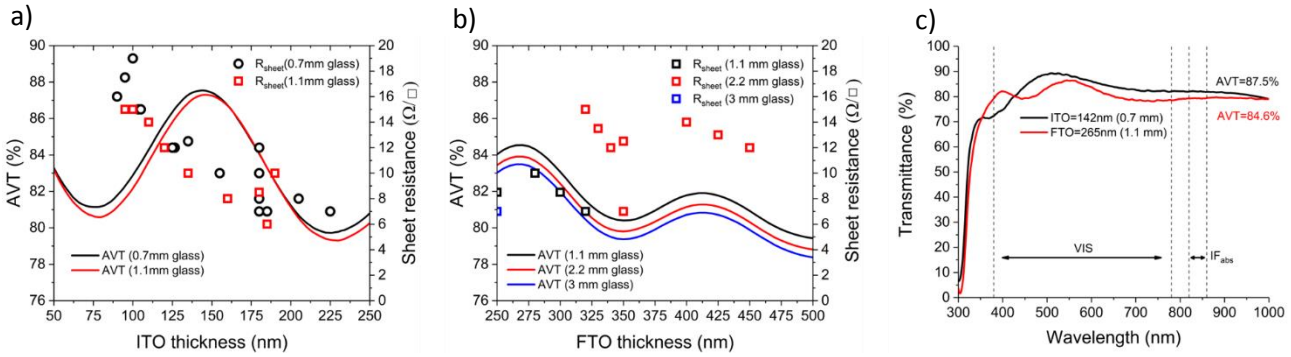

Figure S1: Simulated AVT and corresponding values of sheet resistance extracted from commercial data-sheet for (a) Glass(0.7, 1.1 mm)/SiO_2(20 nm)/ITO(50-250 nm) and (b) Glass(1.1, 2.2, 3 mm)/SnO_2(25 nm)/SiO_2(30 nm)/ITO(250-500 nm). (c) Comparison between transmittance calculated for best the ITO and FTO coated glass substrate.

The TCO data in Figure S2 are based on data sheet of the following glass/TCO producer/vendor

ITO

- MTI Corporation - https://www.mtixtl.com/itocoatedglasssubstrates.aspx
- Crystal-Materials - http://www.crystal-material.com/Substrate-Materials/ITO-coated-glass-conductive.html
- Prazisions Glas & Optik - https://www.pgo-online.com/intl/ito.html
- Sigma-Aldrich - https://www.sigmaaldrich.com/catalog/substance/indiumtinoxidecoatedglassslidesquare123455092611911?lang=it&region=IT
- Techinstro - https://www.techinstro.com/ito-coated-glass/

FTO

- MTI Corporation - https://www.mtixtl.com/ftoglass.aspx
- Techinstro - https://www.techinstro.com/fto-coated-glass/
- MSE Supplies - https://www.msesupplies.com/blogs/products/fto-glass-price-italy
- Crystal-Materials - http://www.crystal-material.com/Substrate-Materials/FTO-coated-glass-conductive.html
- Ossila - https://www.ossila.com/products/fto-glass-unpatterned?variant=21518956481

Optical constants

Figure S3 contains the refractive index and extinction coefficient of both the perovskite and polymer blend used for optical calculations. The bandgap of $MAPbBr_{3-x}Cl_x$ compound is experimentally tuned

by varying the volume ratio between the precursor solutions of $MAPbBr_3$ and $MAPbCl_3$ as 0%, 5%,15%, 20% and 35%.

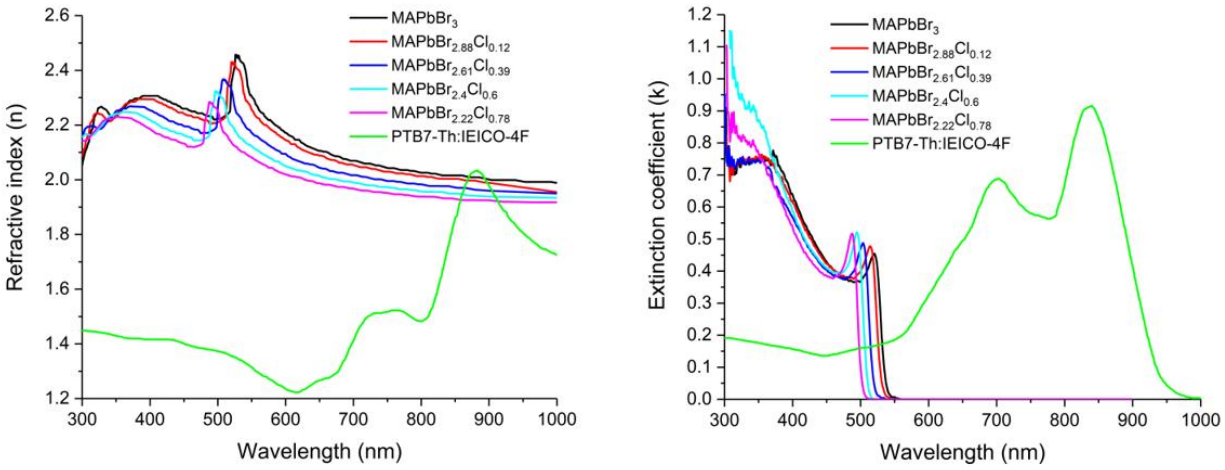

Figure S3: Refractive index (a) and extinction coefficient (b) used in TMM calculations for $MAPbBr_{3-x}Cl_x$ and PTB7-Th:IEICO-4F.

The resulting perovskite compounds show a linear increase of the optical bandgap from 2.33 up to 2.48 eV, and a consequent shift of the wavelength onset from 532 nm to 500 nm as shown in Figure S3(b). The refractive index of each compound is calculated from the $MAPbBr_3$ [1] and $MAPbCl_3$ [2] by using the effective medium approximation theory (EMA). The experimental refractive index and extinction coefficient of the PTB7-Th:IEICO-4F have been reported in Xia et al. work [3].

All the other optical constants used in optical calculations are reported in Figure S4. Panels (a-b) contain the n and k related to materials constituting the ITO and FTO coated glass substrates [4]–[7] and AZO [8], the panels (c-d) parameters related to both the electron and hole transport layers [9]–[13]. At last, panels (d-e) show the optical constants of silver (Ag) [14], lithium fluoride (LiF) [14] and molybdenum trioxide (MoO_3) [14] used in photonic crystal for light management in OSCs.

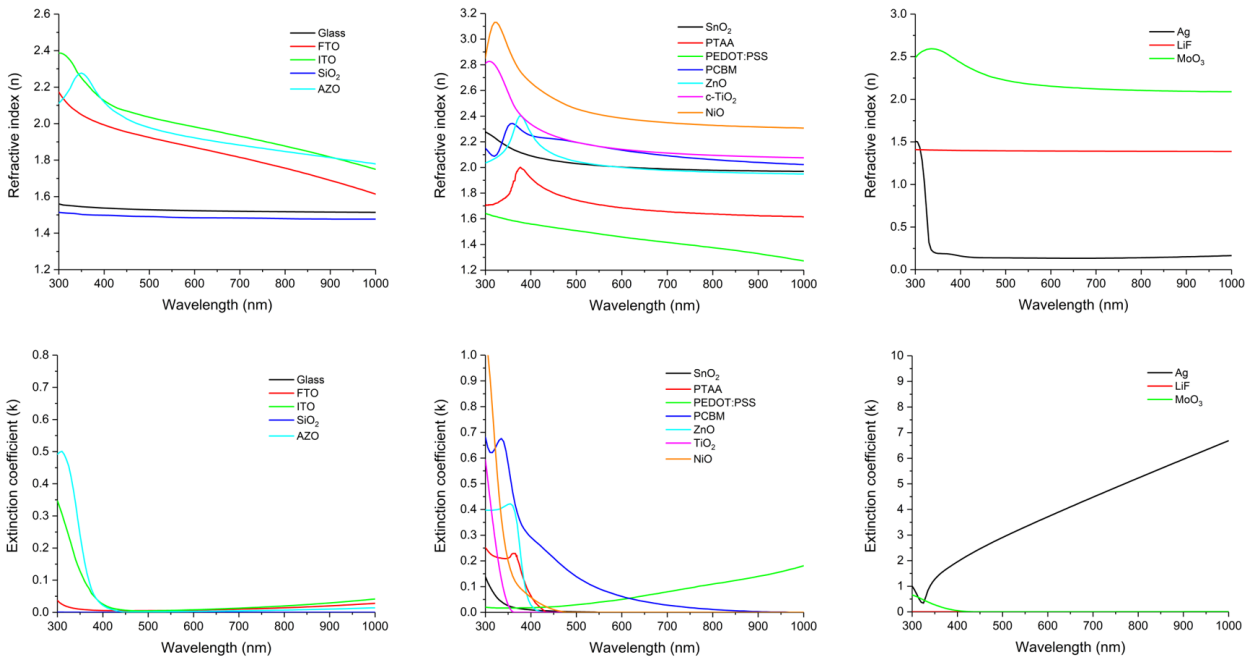

Figure S4: Refractive indices (a-c) and extinction coefficients (d-f) used in TMM calculations to model materials used in TCOs, HTLs, ETLs and PC.

Optical calculations on PSCs

We performed preliminary optical calculations on P-I-N and N-I-P planar PSC architectures, in order to choose the most effective stack in terms of both the AVT and power conversion efficiency (PCE). In particular, for the N-I-P configuration we investigated the effect of different TCO/ETL, including the ITO/SnO_2, FTO/SnO_2 and ITO/TiO_2, while for the P-I-N one we perform the same study by varying the HTL as NiO, PEDOT:PSS and PTAA. In Figure S5 we report the 2D color maps indicating the AVT obtained for the different stacks investigated. Black level curves indicate the ideal J_{SC} (with IQE=100%) achievable depending on the stack dimensioning.

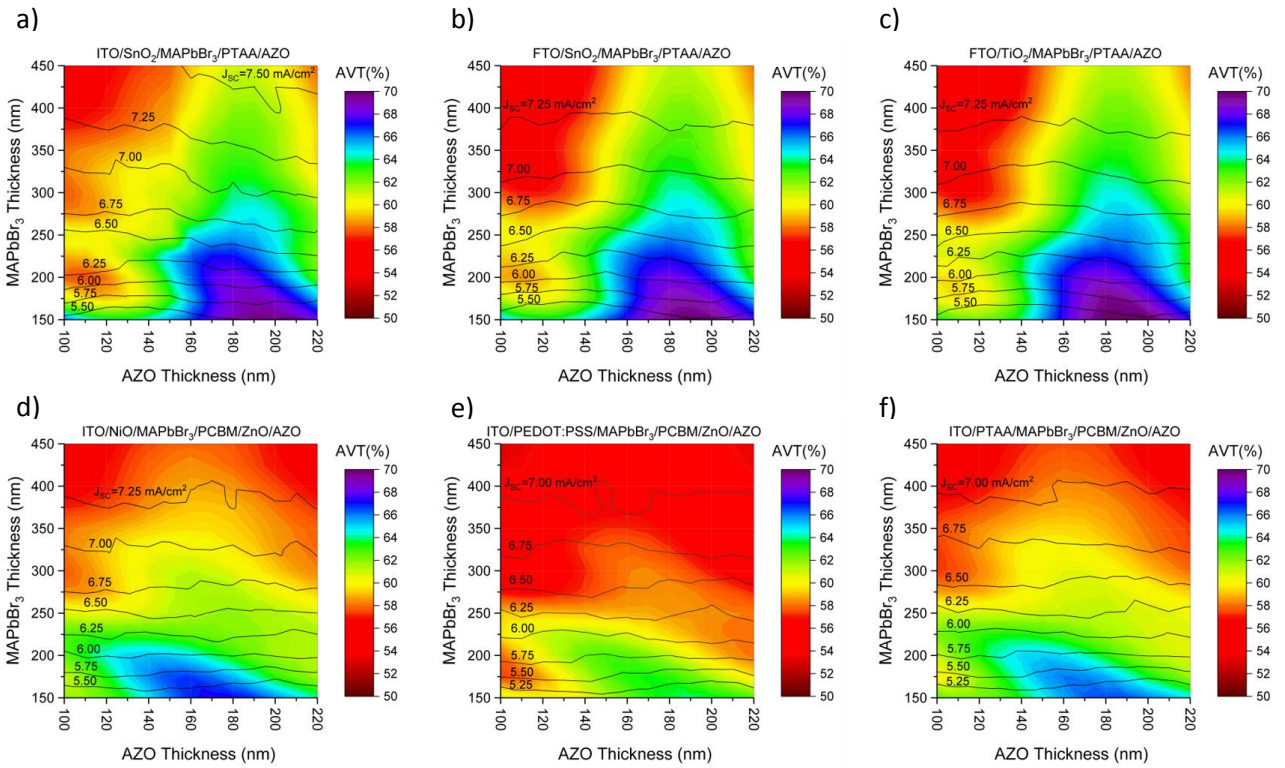

Figure S5: Color maps of AVT depending on the $MAPbBr_3$ and AZO thickness. Black level curves indicate the theoretical J_{SC} photogenerated within the perovskite layer. Panels (a-c) are related to the N-I-P planar architecture for which we varied both the TCO and ETL as follow: ITO/SnO_2, FTO/SnO_2 and ITO/TiO_2. Similarly, panels (d-f) are related to the P-I-N planar architectures for which we varied the HTL as NiO, PEDOT:PSS and PTAA.

Maps depicted in Figure S5(a-c) related to the N-I-P architecture show that the ITO/SnO_2 allows to obtain higher photocurrent and AVT comparable to the others. Whereas maps depicted in Figure S5(d-f) show that the HTL importantly affect the performance of the P-I-N architecture, in fact the use of a very thin NiO (10 nm) allows to achieve good photocurrent keeping high AVT value.

Therefore, the Glass/ITO/SnO_2/$MAPbBr_3$/PTAA/AZO and Glass/ITO/NiO/$MAPbBr_3$/$PC_{60}BM$/ZnO/AZO stacks have been selected for the following optimization steps.

Design and optimization of photonic crystals

The multilayer structure for light management used in OSCs is designed in order to increase at the same time both the AVT and the PCE. This is possible by exploiting the coherent interferences due to the presence of alternating high and low refractive index dielectric materials at final interface of

the structure. Here we compare and evaluate a distributed Bragg reflector (DBR) and a photonic crystal structure [3], both aimed to increase as much as possible the reflection of spectral component at the PTB7-Th:IEICO-4F absorption peak (840 nm) and at same time reducing it within the visible range. The dimensioning of structures depicted in Figure S6a is performed analytically for the DBR, and through TMM [15] calculations for the PC.

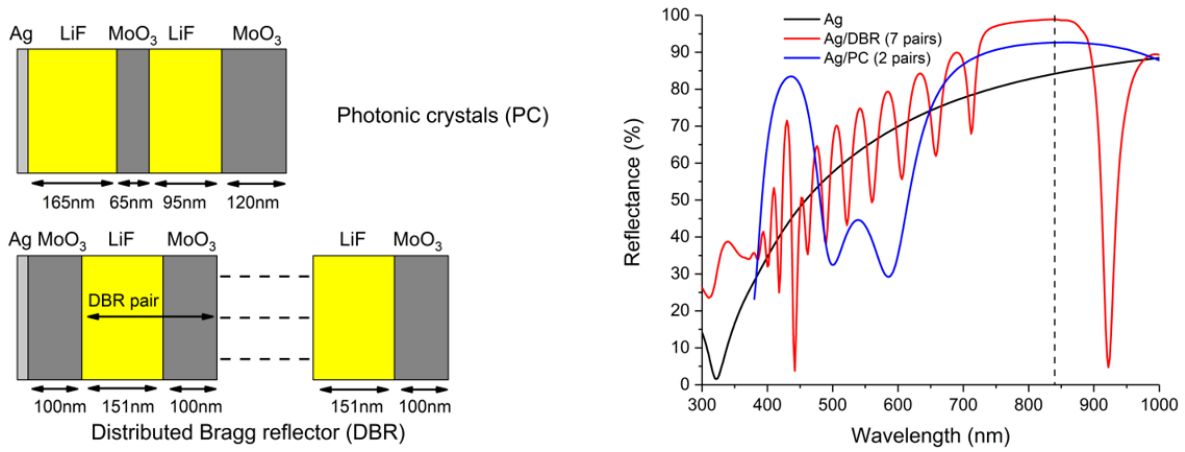

Figure S6: Comparison of: (a) designed DBR and PC structures; (b) reflectance dependency by the addition of DBR (red plot) or PC (blue plot) on a 20nm-thick Ag single layer (black plot). Results were obtained with TMM calculations.

Figure S6b shows the reflectance obtained with TMM calculations for the designed structures compared with a single very thin Ag layer (black plot). Although the DBR structure (red plot) gives the best reflectance at 840 nm it will not provide a substantial increase of AVT due to the harmonics affecting the visible range. On the other hand, the photonic crystal structure shows a better compromise between reflectance magnitude at 840 nm and AVT, indeed the R(λ) within the 450-650 nm results quite reduced. To this end, the use of photonic crystals represents the best choice for this design.

As further confirmation of the importance of the photonic crystal we report in Figure S7 the comparison of AVT and J_{SC} obtained by varying the thickness of the BHJ absorber.

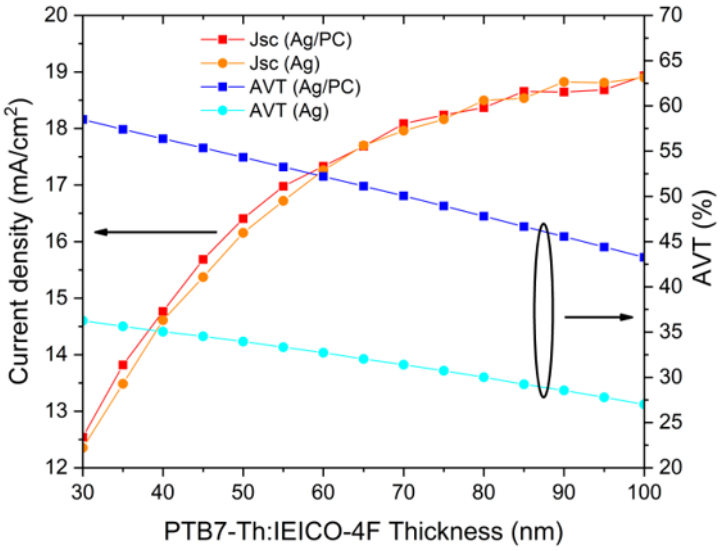

Figure S7: Comparison of short-circuit current density (J_{SC}) and AVT calculated for the OSC with (red and blue plots) and without (cyan and orange plots) photonic crystals (PC).

These results demonstrate that for an unfiltered OSC with thin absorber (below 60nm) the addition of PC principally leads to dramatically increase the AVT of 15-20% and modestly the J_{SC} of 0.1-0.25 mA/cm^2. For thicker absorber the second effect tends to disappear.

Design of anti-reflection coatings

Figure S8(a-b) show the comparison between the target refractive index (black plots) and suitable materials for both the frontal and intermediate anti-reflection coating (ARC). The frontal ARC is aimed to reduce the top surface reflection by exploiting destructive interference phenomena. The intermediate ARC has the double functionality to reduce the reflections between the sub-cells and to ensure the mechanical stacking in the 4T tandem device. The ideal refractive index indicated (n_1) in both plots are determined by using the formula in **Eq. (S1)** such that the optical coupling is maximized.

$$n_1 = \sqrt{n_0 \cdot n_2} \qquad \text{(S1)}$$

Where, n_0 and n_2 represent respectively the previous and next layer to the ARC.

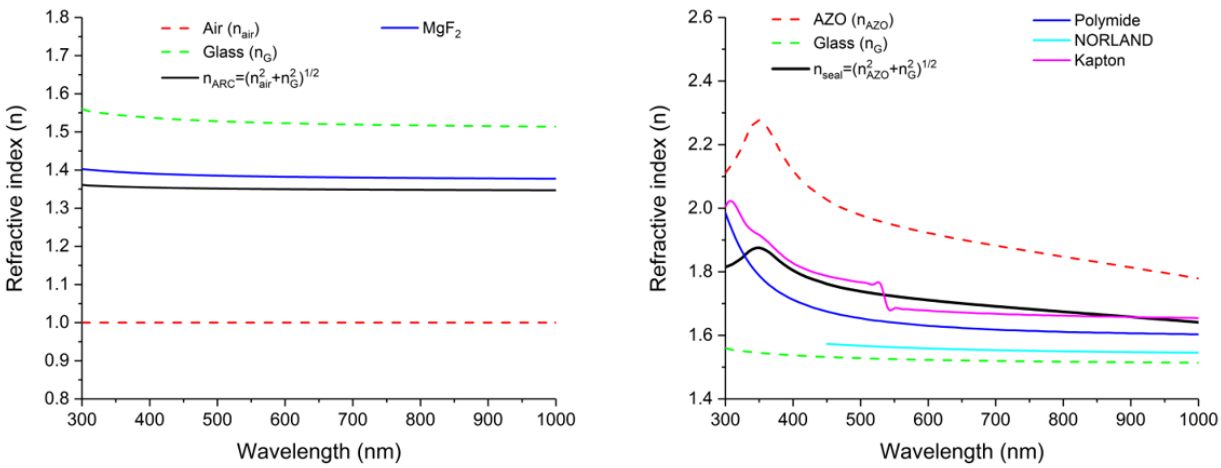

Figure S8: Optical constants of the MgF_2 [16]*, NORLAND, Kapton* [17]*, and Polyimide* [9] *used for the (a) frontal and (b) intermediated ARC employed in tandem structures. In both panel the black plots indicate the ideal refractive index maximizing the optical coupling between the previous and next layer.*

Regarding the frontal ARC (F-ARC), from comparison in the MgF_2 represents the best candidate. For the intermediate ARC (I-ARC), instead, shows two possible candidates such as the Kapton and Polyimide. Although the Kapton shows a better matching with the target function, it is typically available as very thick film sheet (15-100 µm) [18][19], therefore, the polyimide is more suitable also considering its low-temperature processability and adhesive properties [20].

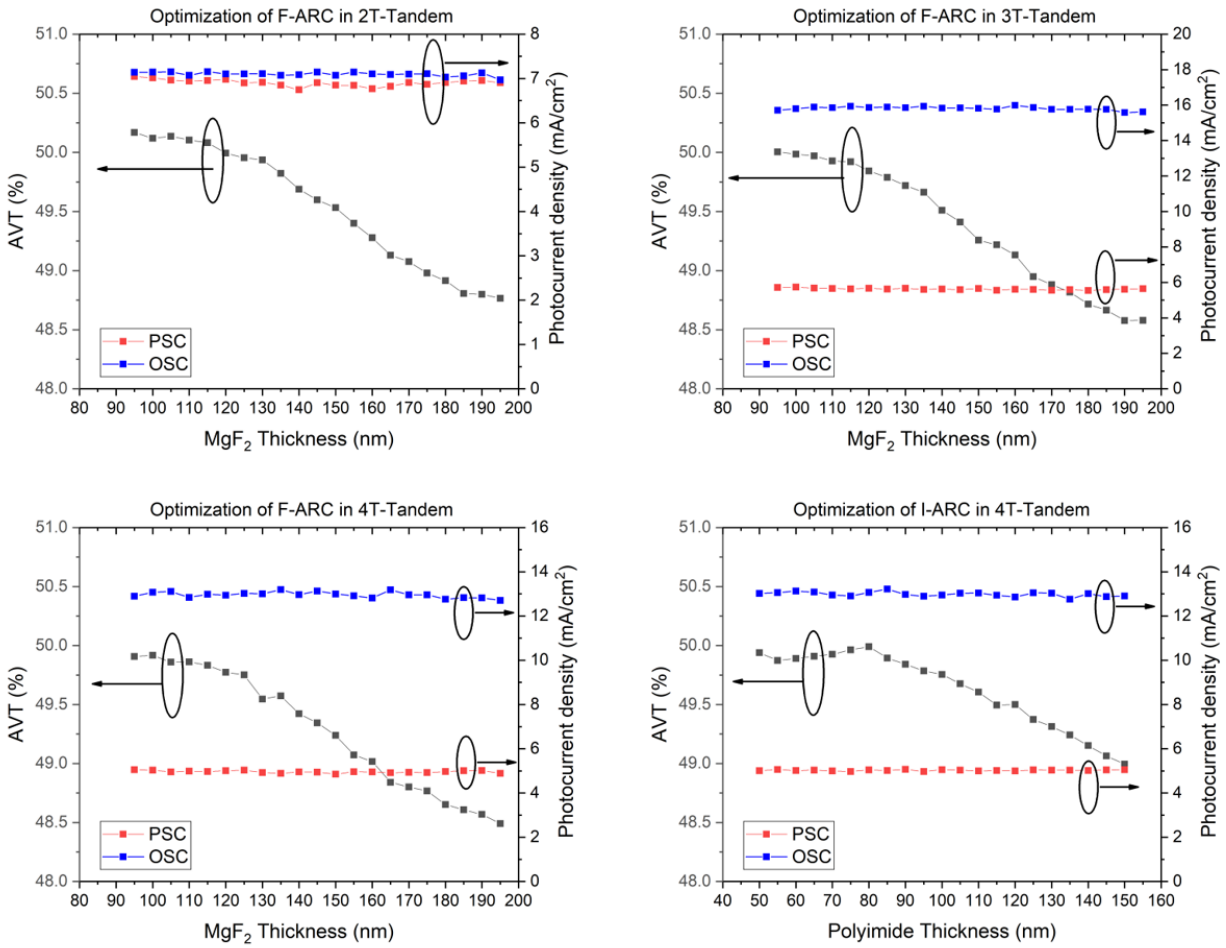

Figure S9: Optimization of the MgF_2 based F-ARC performed by maximizing the AVT for the (a) 2T, (b) 3T and (c) 4T tandem solar cell. (d) Optimization of the Polyimide based I-ARC for the 4T tandem solar cell.

Optimization of the tandem solar cells

Figure S10-S12 and Figure S11 show the evolution of the electro-optical performance for the 2T, 3T and 4T tandem solar cells, respectively. The step-by-step optimization of devices starts from the choice of the perovskite compound ($MAPbBr_{3-x}Cl_x$) and through the implementation of photonic crystals to increase the absorption within the bottom-cell. The last step regards the design of proper frontal and intermediate ARC in order to improve the optical coupling. Notably, due to the limited number of TCOs in the 2T tandem architecture, the use of $MAPbBr_3$ is enough to guarantee AVT>50%, therefore the bandgap tuning optimization step was not performed.

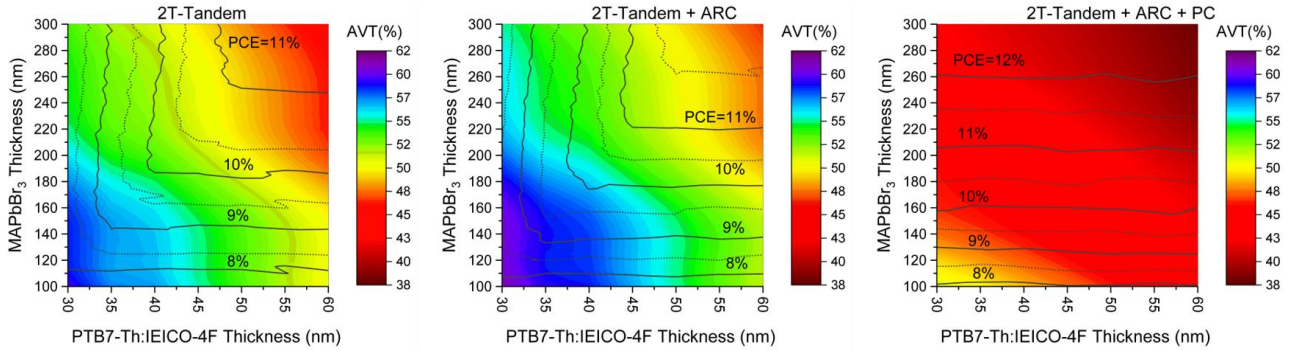

Figure S10: 2D color maps obtained by electro-optical simulations for the 2T tandem solar cell (a) without and (b) with the frontal ARC made with MgF_2. 2D color map in panel (c) shows the dramatic decrease of AVT by replacing the AZO with photonic crystals.

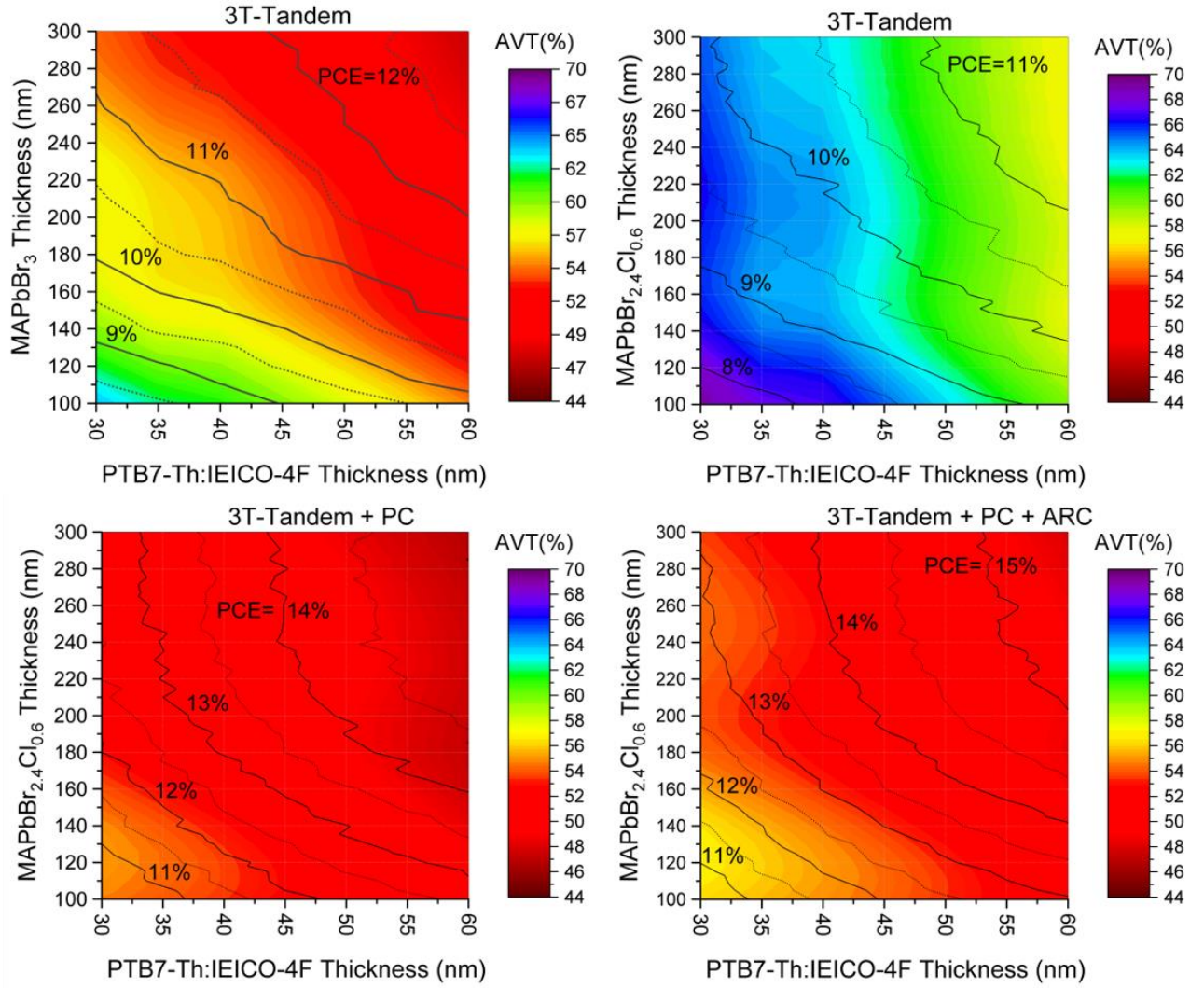

Figure S11: 2D color maps obtained by electro-optical simulations for the 3T tandem solar cell considering: (a) $MAPbBr_3$ as top cell absorber; (b) the inclusion of x=0.20 of chlorine; (c) the use of photonic crystals; (d) the addition of the MgF_2-based frontal ARC.

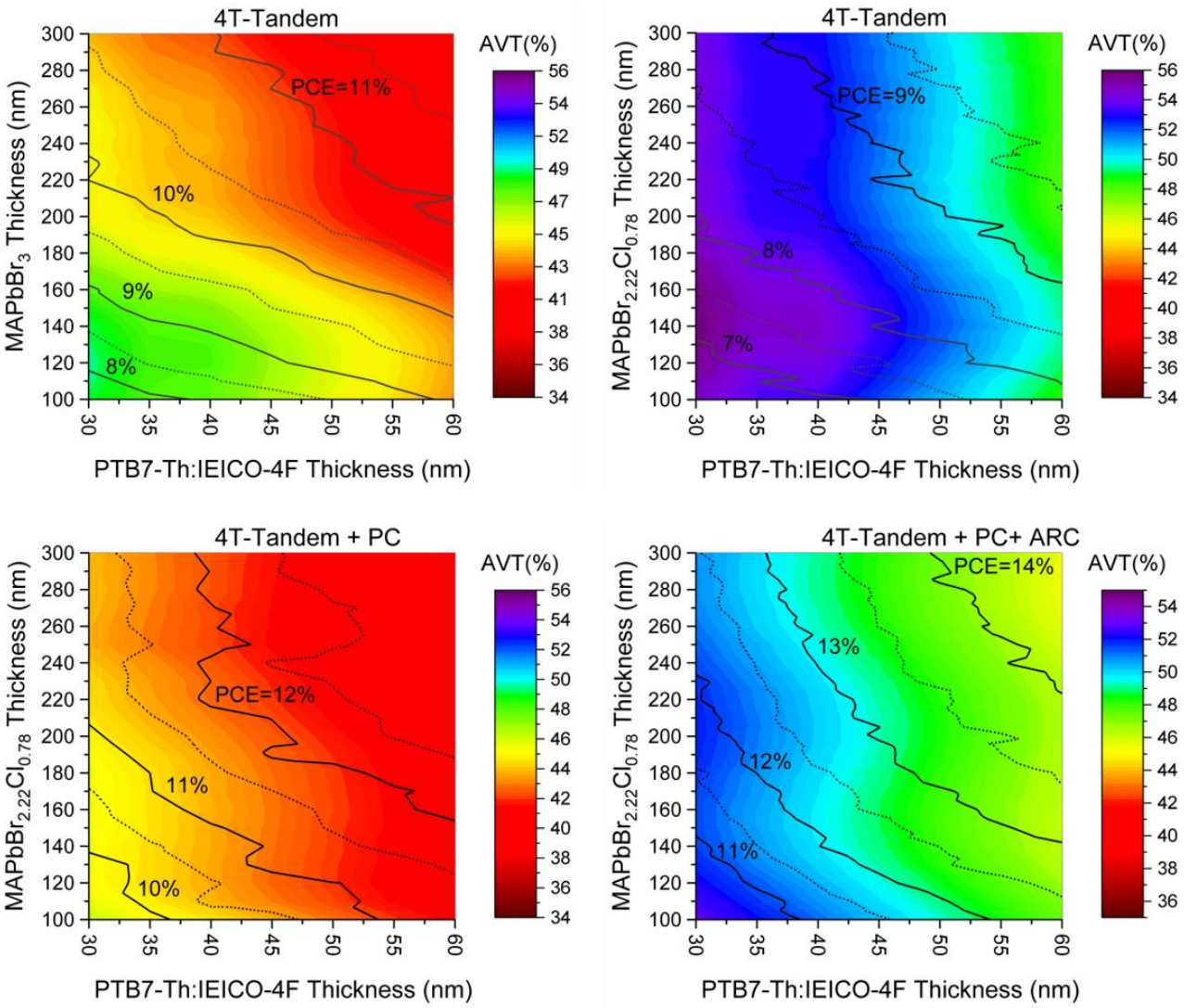

Figure S12: 2D color maps obtained by electro-optical simulations for the 4T tandem solar cell considering: (a) $MAPbBr_3$ as top cell absorber; (b) the inclusion of x=0.26 of chlorine; (c) the use of photonic crystals; (d) the addition of both the frontal and intermediate ARC, respectively made with MgF_2 and Polyimide.

In Table S1 we report the stack related to the 2D color maps depicted in Figure S10, S11, S12.

Table S1: Summary of device stacks used for the design of the 2T, 3T and 4T tandem solar cell during the design workflow step-by-step as shown in Figure S10, S11, S12.

Terminals:	Step:	Cell:	Device stack:
2T	x=0	Top: Bottom:	Glass/SiO_2/ITO/NiO/$MAPbBr_3$/$PC_{60}BM$/ZnO/AZO + PEDOT:PSS/PTB7-Th:IEICO-4F/ZnO/AZO
	ARC	Top: Bottom:	MgF_2/Glass/SiO_2/ITO/NiO/$MAPbBr_3$/$PC_{60}BM$/ZnO/AZO + PEDOT:PSS/PTB7-Th:IEICO-4F/ZnO/AZO
	PC	Top: Bottom:	MgF_2/Glass/SiO_2/ITO/NiO/$MAPbBr_3$/$PC_{60}BM$/ZnO/AZO + PEDOT:PSS/PTB7-Th:IEICO-4F/ZnO/Ag/PC
3T	x=0	Top: Bottom:	Glass/SiO_2/ITO/SnO_2/$MAPbBr_3$/PTAA/AZO + PEDOT:PSS/PTB7-Th:IEICO-4F/ZnO/AZO
	x=0.6	Top: Bottom:	Glass/SiO_2/ITO/SnO_2/$MAPbBr_{2.4}Cl_{0.6}$/PTAA/AZO + PEDOT:PSS/PTB7-Th:IEICO-4F/ZnO/AZO
	PC	Top: Bottom:	Glass/SiO_2/ITO/SnO_2/$MAPbBr_{2.4}Cl_{0.6}$/PTAA/AZO + PEDOT:PSS/PTB7-Th:IEICO-4F/ZnO/Ag/PC
	ARC	Top: Bottom:	MgF_2/Glass/SiO_2/ITO/SnO_2/$MAPbBr_3$/PTAA/AZO + PEDOT:PSS/PTB7-Th:IEICO-4F/ZnO/Ag/PC
4T	x=0	Top: Bottom:	Glass/SiO_2/ITO/NiO/$MAPbBr_3$/$PC_{60}BM$/ZnO/AZO/Air/ + Air/Glass/SiO_2/ITO/PEDOT:PSS/PTB7-Th:IEICO-4F/ZnO/AZO
	x=0.78	Top: Bottom:	Glass/SiO_2/ITO/NiO/$MAPbBr_{2.22}Cl_{0.78}$/$PC_{60}BM$/ZnO/AZO/Air + Air/Glass/SiO_2/ITO/PEDOT:PSS/PTB7-Th:IEICO-4F/ZnO/AZO
	PC	Top: Bottom:	Glass/SiO_2/ITO/NiO/$MAPbBr_{2.22}Cl_{0.78}$/$PC_{60}BM$/ZnO/AZO/ Air + Air/Glass/SiO_2/ITO/PEDOT:PSS/PTB7-Th:IEICO-4F/ZnO/Ag/PC
	ARC	Top: Bottom:	MgF_2/Glass/SiO_2/ITO/NiO/$MAPbBr_{2.22}Cl_{0.78}$/$PC_{60}BM$/ZnO/AZO/PI + PI/Glass/SiO_2/ITO/PEDOT:PSS/PTB7-Th:IEICO-4F/ZnO/Ag/PC

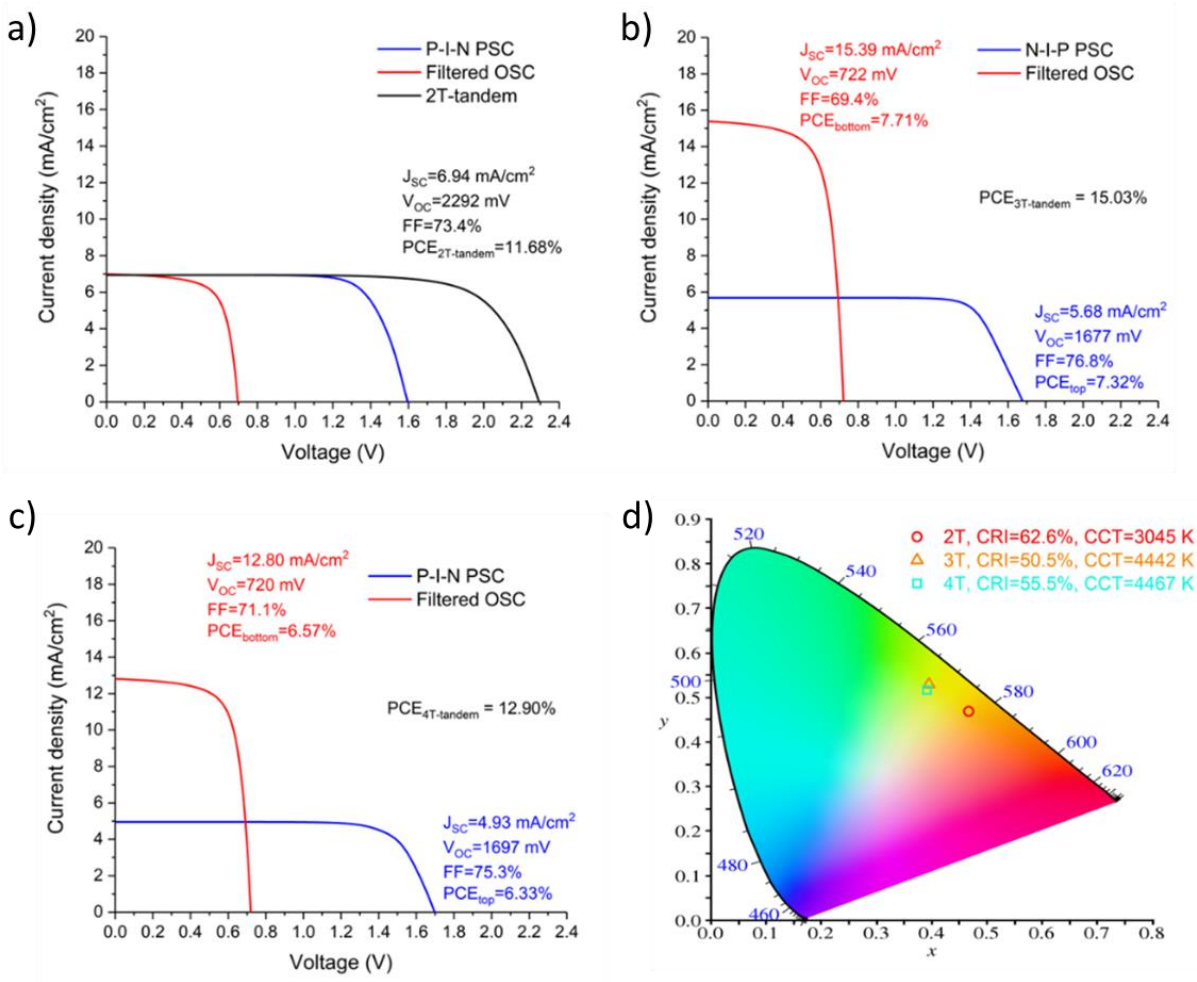

Figure S13: (a-c) JV characteristics obtained with DD simulations for the 2T, 3T and 4T tandem solar cells, including the calculated individual/global performance. (d) CIE xy chromaticity diagram indicating the color appearance obtained for designed devices with AVT=50% and including the related estimated CRI and CCT.

Color Rendering Index and Correlated Color Temperature

The aesthetical properties of designed devices are evaluated by calculating their color rendering index (CRI) and correlated color temperature (CCT) [21], since both of them describe the nature of the light source under different concepts. The first parameter indicates the ability of the light to display all the wavelengths of natural sunlight spectrum, as compared to the color temperature, therefore, the lower the CRI the less the source, or in our case the light transmission, reproduces the natural sunlight. The CCT, instead, determines the color characteristic of the light, where temperatures around 2700 K

indicate the warm and around 5000 K the cool color, thus values intermediate allow to have a neutral light.

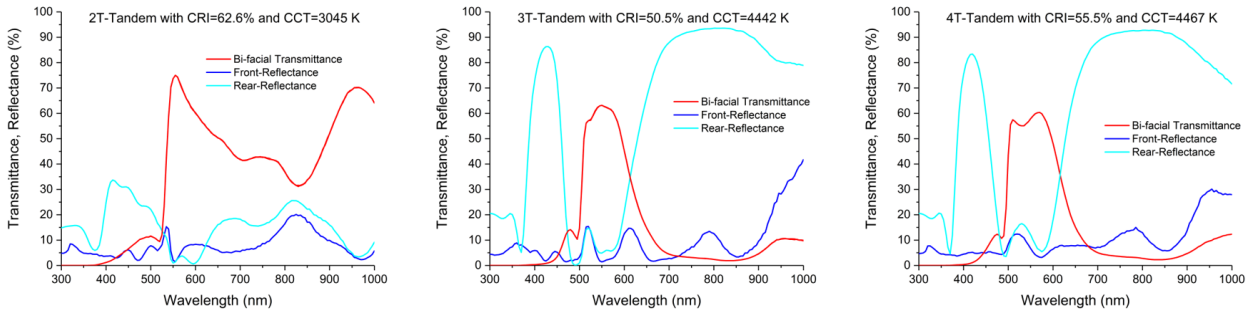

Figure S14: Bi-facial transmittance (red), frontal (blue) and rear reflectance (cyan) obtained for the best (a) 2T, (b) 3T and (c) 4T tandem device and used to calculate the CRI and CCT.

Electrical parameters for DD model

Table S2: Electrical parameters used in both the P-I-N and N-I-P PSC device simulations.

	P-I-N PSC			**N-I-P PSC**		
Layer	**Material**	**Parameter**	**Value**	**Material**	**Parameter**	**Value**
Anode	AZO:PVP	Work function [eV]	-4.5 [22]	ITO	Work function [eV]	-4.7 [23]
ETL	ZnO	CB [eV] VB [eV] μ_n, μ_p [$cm^2\ V^{-1}\ s^{-1}$] Permittivity	-4.3 [24] -7.4 [24] 1, 1 [25] 8.5 [25]	SnO_2	CB [eV] VB [eV] μ_n, μ_p [$cm^2\ V^{-1}\ s^{-1}$] Permittivity	-4.1 [26] -8.4 [26] 5, 1 [27] 14 [28]
HBL	$PC_{60}BM$	LUMO [eV] HOMO [eV] μ_n, μ_p [$cm^2\ V^{-1}\ s^{-1}$] Permittivity	-4.0 [29] -6.1 [29] 10^{-4}, 10^{-4} [30] 3.9 [31]	-	-	-
Absorber	$MAPbBr_3$	CB [eV] VB [eV] μ_n, μ_p [$cm^2\ V^{-1}\ s^{-1}$] Permittivity Direct rec. [$cm^3\ s^{-1}$] τ_n, τ_p [ns] Trap density [cm^{-3}]	-3.4 [32] -5.7 c 8.6, 9 [33] 25.5 [34] 5×10^{-10} [35], [36] 100, 100 3.5×10^{15} [37]	$MAPbBr_3$	CB [eV] VB [eV] μ_n, μ_p [$cm^2\ V^{-1}\ s^{-1}$] Permittivity Direct rec. [$cm^3\ s^{-1}$] τ_n, τ_p [ns] Trap density [cm^{-3}]	-3.4 [32] -5.7 [32] 8.6, 9 [33] 25.5 [34] 5×10^{-10} [35], [36] 100, 100 3.5×10^{15} [37]
HTL	NiO	CB [eV] VB [eV] μ_n, μ_p [$cm^2\ V^{-1}\ s^{-1}$] Permittivity	-1.8 [23] -5.4 [23] 10^{-2}, 10^{-2} [38] 11 [39]	PTAA	LUMO [eV] HOMO [eV] μ_n, μ_p [$cm^2\ V^{-1}\ s^{-1}$] Permittivity	-2.2 [40] -5.2 [40] 10^{-3}, 10^{-3} [41] 3.5 [42]
Cathode	ITO	Work function [eV]	-5.0 [23]	AZO	Work function [eV]	-4.9 [22]

Table S 3: Electrical parameters used in DD simulations for the OSC.

OSC			
Layer	**Material**	**Parameter**	**Value**
Cathode	ITO	Work function [eV]	-5.0 [23]
HTL	PEDOT:PSS	LUMO [eV] HOMO [eV]	-3.5 [43] -5.2 [43]

		μ_n, μ_p [cm^2 V^{-1} s^{-1}] Permittivity	1, 0.3 [44] 3 [45]
BHJ	PTB7-Th:IEICO-4F	LUMO [eV] HOMO [eV] μ_n, μ_p [cm^2 V^{-1} s^{-1}] Permittivity Direct rec. [cm^3 s^{-1}]	-4.19 [46] -5.24 [46] 9.35×10^{-5}, 4.56×10^{-5} [46] 3 2×10^{-13} [12]
ETL	ZnO	CB [eV] VB [eV] μ_n, μ_p [cm^2 V^{-1} s^{-1}] Permittivity	-4.3 [24] -7.4 [24] 1, 1 [25] 8.5 [25]
Opaque anode	Ag	Work function [eV]	-4.7 [22]
Transparent anode	AZO	Work function [eV]	-4.5 [22]

Device simulations are performed by using the drift-diffusion simulation tool TiberCAD [47]. Table S2 and Table S 3 contain the full list of electrical parameters used for the PSCs and OSCs. The charge transport calculation is performed by consistently including the generation rate profile carried out through TMM. According with experimental results reported in literature for ITO and AZO based transparent contacts [22], [23], we set different value of work function depending if they represent the n or p contact.

The electrical parameters of the methylammonium lead bromide/chloride ($MAPbBr_{3-x}Cl_x$) compound used to enhance the transparency of the top cell in the 3T and 4T tandem devices are obtained by linear interpolation from parameters collected for the $MAPbBr_3$ and $MAPbCl_3$. In Table S4 we summarize the electrical parameters considered for each perovskite variation depending on the chlorine addition (x).

Table S4: Electrical parameters of $MAPbBr_{3-x}Cl_x$, such as energy levels and carrier mobility, estimated by linear interpolation. The energy gap values are experimentally extracted from extinction coefficients depicted in Figure S3.

Parameter	**$MAPbBr_3$**	**$MAPbBr_{2.88}Cl_{0.12}$**	**$MAPbBr_{2.61}Cl_{0.39}$**	**$MAPbBr_{2.4}Cl_{0.6}$**	**$MAPbBr_{2.22}Cl_{0.78}$**	**$MAPbCl_3$**
CB [eV]	-3.40 [32]	-3.38	-3.34	-3.31	-3.28	-2.82 [48]
VB [eV]	-5.70 [32]	-5.70	-5.71	-5.72	-5.73	-5.82 [48]
Energy gap [eV]	2.3 [32]	2.32	2.37	2.41	2.45	3.0 [48]
μ_n, μ_p [cm^2 V^{-1} s^{-1}]	8.6, 9 [33]	8.5, 8.9	8, 8.4	7.7, 8	7.4, 7.7	4, 4 [49]

References

[1] P. F. Ndione, Z. Li, and K. Zhu, "Effects of alloying on the optical properties of organic–inorganic lead halide perovskite thin films," *J. Mater. Chem. C*, vol. 4, no. 33, pp. 7775–7782, 2016, doi: 10.1039/C6TC02135B.

[2] M. Kato *et al.*, "Universal rules for visible-light absorption in hybrid perovskite materials," *J. Appl. Phys.*, vol. 121, no. 11, p. 115501, Mar. 2017, doi: 10.1063/1.4978071.

[3] R. Xia, C. J. Brabec, H.-L. Yip, and Y. Cao, "High-Throughput Optical Screening for Efficient Semitransparent Organic Solar Cells," *Joule*, vol. 3, no. 9, pp. 2241–2254, Sep. 2019, doi: 10.1016/j.joule.2019.06.016.

[4] D. S. Bhachu, M. R. Waugh, K. Zeissler, W. R. Branford, and I. P. Parkin, "Textured Fluorine-Doped Tin Dioxide Films formed by Chemical Vapour Deposition," *Chem. - A Eur. J.*, vol. 17, no. 41, pp. 11613–11621, Oct. 2011, doi: 10.1002/chem.201100399.

[5] H. Fujiwara and M. Kondo, "Effects of carrier concentration on the dielectric function of ZnO:Ga and In 2O 3:Sn studied by spectroscopic ellipsometry: Analysis of free-carrier and band-edge absorption," *Phys. Rev. B - Condens. Matter Mater. Phys.*, vol. 71, no. 7, p. 075109, Feb. 2005, doi: 10.1103/PhysRevB.71.075109.

[6] J. M. Ball *et al.*, "Optical properties and limiting photocurrent of thin-film perovskite solar cells," *Energy Environ. Sci.*, vol. 8, no. 2, pp. 602–609, 2015, doi: 10.1039/C4EE03224A.

[7] L. Gao, F. Lemarchand, and M. Lequime, "Refractive index determination of SiO_2 layer in the UV/Vis/NIR range: spectrophotometric reverse engineering on single and bi-layer designs," *J. Eur. Opt. Soc. Rapid Publ.*, vol. 8, p. 13010, Jan. 2013, doi: 10.2971/jeos.2013.13010.

[8] T. Hara, T. Maekawa, S. Minoura, Y. Sago, S. Niki, and H. Fujiwara, "Quantitative assessment of optical gain and loss in submicron-textured CuIn1-xGaxSe2 solar cells fabricated by three-stage coevaporation," *Phys. Rev. Appl.*, vol. 2, no. 3, p. 034012, Sep. 2014, doi: 10.1103/PhysRevApplied.2.034012.

[9] M. Campoy-Quiles, J. Nelson, D. D. C. Bradley, and P. G. Etchegoin, "Dimensionality of electronic excitations in organic semiconductors: A dielectric function approach," *Phys. Rev. B*, vol. 76, no. 23, p. 235206, Dec. 2007, doi: 10.1103/PhysRevB.76.235206.

[10] H. S. So, J.-W. Park, D. H. Jung, K. H. Ko, and H. Lee, "Optical properties of amorphous and crystalline Sb-doped SnO 2 thin films studied with spectroscopic ellipsometry: Optical gap energy and effective mass," *J. Appl. Phys.*, vol. 118, no. 8, p. 085303, Aug. 2015, doi: 10.1063/1.4929487.

[11] H. L. Lu, G. Scarel, M. Alia, M. Fanciulli, S.-J. Ding, and D. W. Zhang, "Spectroscopic ellipsometry study of thin NiO films grown on Si (100) by atomic layer deposition," *Appl. Phys. Lett.*, vol. 92, no. 22, p. 222907, Jun. 2008, doi: 10.1063/1.2938697.

[12] J. Wang *et al.*, "Ultra-narrow bandgap non-fullerene organic solar cells with low voltage losses and a large photocurrent," *J. Mater. Chem. A*, vol. 6, no. 41, pp. 19934–19940, 2018, doi: 10.1039/C8TA07954D.

[13] L. A. . Pettersson, S. Ghosh, and O. Inganäs, "Optical anisotropy in thin films of poly(3,4-ethylenedioxythiophene)–poly(4-styrenesulfonate)," *Org. Electron.*, vol. 3, no. 3–4, pp. 143–148, Dec. 2002, doi: 10.1016/S1566-1199(02)00051-4.

[14] H. Fujiwara and R. W. Collins, Eds., *Spectroscopic Ellipsometry for Photovoltaics*, vol. 214. Cham: Springer International Publishing, 2018.

[15] M. C. Troparevsky, A. S. Sabau, A. R. Lupini, and Z. Zhang, "Transfer-matrix formalism for the calculation of optical response in multilayer systems: from coherent to incoherent interference," *Opt. Express*, vol. 18, no. 24, p. 24715, Nov. 2010, doi: 10.1364/OE.18.024715.

[16] L. V. Rodríguez-de Marcos, J. I. Larruquert, J. A. Méndez, and J. A. Aznárez, "Self-consistent optical constants of MgF_2, LaF_3, and CeF_3 films," *Opt. Mater. Express*, vol. 7, no. 3, p. 989, Mar. 2017, doi: 10.1364/OME.7.000989.

[17] E. T. Arakawa, M. W. Williams, J. C. Ashley, and L. R. Painter, "The optical properties of Kapton: Measurement and applications," *J. Appl. Phys.*, vol. 52, no. 5, pp. 3579–3582, May 1981, doi: 10.1063/1.329140.

[18] "Electron Microscopy Sciences," *Kapton® Polyimide Film Tape*. [Online]. Available: https://www.emsdiasum.com/microscopy/technical/datasheet/77708.aspx.

[19] "Dupont Kapton," *DuPont Kapton® HN General Purpose Polyimide Film Sheet*. [Online]. Available: https://www.eis-inc.com/polyimide-film/p-ph21-kapton hn-sht.

[20] I. Mathews, D. O'Mahony, K. Thomas, E. Pelucchi, B. Corbett, and A. P. Morrison, "Adhesive bonding for mechanically stacked solar cells," *Prog. Photovoltaics Res. Appl.*, vol. 23, no. 9, pp. 1080–1090, Sep. 2015, doi: 10.1002/pip.2517.

[21] A. R. Robertson, "Computation of Correlated Color Temperature and Distribution Temperature," *J. Opt. Soc. Am.*, vol. 58, no. 11, p. 1528, Nov. 1968, doi: 10.1364/JOSA.58.001528.

[22] X. Yu, X. Yu, J. Zhang, D. Zhang, H. Cai, and Y. Zhao, "Interfacial modification for improving inverted organic solar cells by poly(N-vinylpyrrolidone)," *RSC Adv.*, vol. 5, no. 73, pp. 58966–58972, 2015, doi: 10.1039/C5RA09427E.

[23] Y. Sun, W. Chen, Y. Wu, Z. He, S. Zhang, and S. Chen, "A low-temperature-annealed and UV-ozone-enhanced combustion derived nickel oxide hole injection layer for flexible quantum dot light-emitting diodes," *Nanoscale*, vol. 11, no. 3, pp. 1021–1028, 2019, doi: 10.1039/C8NR08976K.

[24] Y. Qin *et al.*, "Highly Efficient Fullerene-Free Polymer Solar Cells Fabricated with Polythiophene Derivative," *Adv. Mater.*, vol. 28, no. 42, pp. 9416–9422, Nov. 2016, doi: 10.1002/adma.201601803.

[25] Z.-L. Tseng, C.-H. Chiang, S.-H. Chang, and C.-G. Wu, "Surface engineering of ZnO electron transporting layer via Al doping for high efficiency planar perovskite solar cells," *Nano Energy*, vol. 28, pp. 311–318, Oct. 2016, doi: 10.1016/j.nanoen.2016.08.035.

[26] Z. Xu *et al.*, "La-doped SnO2 as ETL for efficient planar-structure hybrid perovskite solar cells," *Org. Electron.*, vol. 73, pp. 62–68, Oct. 2019, doi: 10.1016/j.orgel.2019.03.053.

[27] L. Xiong *et al.*, "Performance enhancement of high temperature SnO 2 -based planar perovskite solar cells: electrical characterization and understanding of the mechanism," *J. Mater. Chem. A*, vol. 4, no. 21, pp. 8374–8383, 2016, doi: 10.1039/C6TA01839D.

[28] D. M. Roessler and W. A. Albers, "Infrared reflectance of single crystal tetragonal GeO2," *J. Phys. Chem. Solids*, vol. 33, no. 2, pp. 293–296, Jan. 1972, doi: 10.1016/0022-3697(72)90010-8.

[29] C. M. Wolff, F. Zu, A. Paulke, L. P. Toro, N. Koch, and D. Neher, "Reduced Interface-Mediated Recombination for High Open-Circuit Voltages in CH 3 NH 3 PbI 3 Solar Cells," *Adv. Mater.*, vol. 29, no. 28, p. 1700159, Jul. 2017, doi: 10.1002/adma.201700159.

[30] P.-W. Liang, C.-C. Chueh, S. T. Williams, and A. K.-Y. Jen, "Roles of Fullerene-Based Interlayers in Enhancing the Performance of Organometal Perovskite Thin-Film Solar Cells," *Adv. Energy Mater.*, vol. 5, no. 10, p. 1402321, May 2015, doi: 10.1002/aenm.201402321.

[31] H. Sun *et al.*, "Ionization Energies, Electron Affinities, and Polarization Energies of Organic Molecular Crystals: Quantitative Estimations from a Polarizable Continuum Model (PCM)-Tuned Range-Separated Density Functional Approach," *J. Chem. Theory Comput.*, vol. 12, no. 6, pp. 2906–2916, Jun. 2016, doi: 10.1021/acs.jctc.6b00225.

[32] S. Ryu *et al.*, "Voltage output of efficient perovskite solar cells with high open-circuit voltage and fill factor," *Energy Environ. Sci.*, vol. 7, no. 8, pp. 2614–2618, 2014, doi: 10.1039/C4EE00762J.

[33] C. Li *et al.*, "Halide-Substituted Electronic Properties of Organometal Halide Perovskite Films: Direct and Inverse Photoemission Studies," *ACS Appl. Mater. Interfaces*, vol. 8, no. 18, pp. 11526–11531, May 2016, doi: 10.1021/acsami.6b02692.

[34] M. I. Saidaminov *et al.*, "High-quality bulk hybrid perovskite single crystals within minutes by inverse temperature crystallization," *Nat. Commun.*, vol. 6, no. 1, p. 7586, Nov. 2015, doi: 10.1038/ncomms8586.

[35] P. Ščajev, S. Miasojedovas, and S. Juršėnas, "A carrier density dependent diffusion coefficient, recombination rate and diffusion length in MAPbI 3 and MAPbBr 3 crystals measured under one- and two-photon excitations," *J. Mater. Chem. C*, vol. 8, no. 30, pp. 10290–10301, 2020, doi: 10.1039/D0TC02283G.

[36] X. Chen, H. Lu, Y. Yang, and M. C. Beard, "Excitonic Effects in Methylammonium Lead Halide Perovskites," *J. Phys. Chem. Lett.*, vol. 9, no. 10, pp. 2595–2603, May 2018, doi: 10.1021/acs.jpclett.8b00526.

[37] A. R. Srimath Kandada *et al.*, "Nonlinear Carrier Interactions in Lead Halide Perovskites and the Role of Defects," *J. Am. Chem. Soc.*, vol. 138, no. 41, pp. 13604–13611, Oct. 2016, doi: 10.1021/jacs.6b06463.

[38] J. Zhang *et al.*, "Solution-processed Sr-doped NiOx as hole transport layer for efficient and stable perovskite solar cells," *Sol. Energy*, vol. 174, pp. 1133–1141, Nov. 2018, doi: 10.1016/j.solener.2018.10.004.

[39] A. Kashir, H.-W. Jeong, G.-H. Lee, P. Mikheenko, and Y. H. Jeong, "Dielectric Properties of Strained Nickel Oxide Thin Films," *J. Korean Phys. Soc.*, vol. 74, no. 10, pp. 984–988, May 2019, doi: 10.3938/jkps.74.984.

[40] J. Endres *et al.*, "Electronic structure of the CsPbBr 3 /polytriarylamine (PTAA) system," *J. Appl. Phys.*, vol. 121, no. 3, p. 035304, Jan. 2017, doi: 10.1063/1.4974471.

[41] W. Zhang *et al.*, "Systematic Improvement in Charge Carrier Mobility of Air Stable Triarylamine Copolymers," *J. Am. Chem. Soc.*, vol. 131, no. 31, pp. 10814–10815, Aug. 2009, doi: 10.1021/ja9034818.

[42] Y. Deng *et al.*, "Reduced Self-Doping of Perovskites Induced by Short Annealing for Efficient Solar Modules," *Joule*, vol. 4, no. 9, pp. 1949–1960, Sep. 2020, doi: 10.1016/j.joule.2020.07.003.

[43] M. D. Irwin, D. B. Buchholz, A. W. Hains, R. P. H. Chang, and T. J. Marks, “p-Type semiconducting nickel oxide as an efficiency-enhancing anode interfacial layer in polymer bulk-heterojunction solar cells,” *Proc. Natl. Acad. Sci.*, vol. 105, no. 8, pp. 2783–2787, Feb. 2008, doi: 10.1073/pnas.0711990105.

[44] Y.-J. Lin, J.-Y. Lee, and S.-M. Chen, “Changing electrical properties of PEDOT:PSS by incorporating with dimethyl sulfoxide,” *Chem. Phys. Lett.*, vol. 664, pp. 213–218, Nov. 2016, doi: 10.1016/j.cplett.2016.10.038.

[45] S. W. Tsang, S. C. Tse, K. L. Tong, and S. K. So, “PEDOT:PSS polymeric conducting anode for admittance spectroscopy,” *Org. Electron.*, vol. 7, no. 6, pp. 474–479, Dec. 2006, doi: 10.1016/j.orgel.2006.06.002.

[46] X. Song *et al.*, “Controlling Blend Morphology for Ultrahigh Current Density in Nonfullerene Acceptor-Based Organic Solar Cells,” *ACS Energy Lett.*, vol. 3, no. 3, pp. 669–676, Mar. 2018, doi: 10.1021/acsenergylett.7b01266.

[47] M. Auf Der Maur, G. Penazzi, G. Romano, F. Sacconi, A. Pecchia, and A. Di Carlo, “The multiscale paradigm in electronic device simulation,” *IEEE Trans. Electron Devices*, 2011, doi: 10.1109/TED.2011.2114666.

[48] H.-P. Hsu, L.-C. Li, M. Shellaiah, and K. W. Sun, “Structural, Photophysical, and Electronic Properties of CH3NH3PbCl3 Single Crystals,” *Sci. Rep.*, vol. 9, no. 1, p. 13311, Dec. 2019, doi: 10.1038/s41598-019-49926-z.

[49] G. Maculan *et al.*, “CH 3 NH 3 PbCl 3 Single Crystals: Inverse Temperature Crystallization and Visible-Blind UV-Photodetector,” *J. Phys. Chem. Lett.*, vol. 6, no. 19, pp. 3781–3786, Oct. 2015, doi: 10.1021/acs.jpclett.5b01666.